Cosmogenic [10]Be in pyroxene: laboratory progress, production rate systematics, and application of the [10]Be-[3]He nuclide pair in the Antarctic Dry Valleys

Allie Balter-Kennedy[1,2], Joerg M. Schaefer[1,2], Roseanne Schwartz[1], Jennifer L. Lamp[1], Laura Penrose[1], Jennifer Middleton[1], Bouchaïb Tibari[3], Pierre-Henri Blard[3], Gisela Winckler[1,2], Alan J. Hidy[4], Greg Balco[5]

[1]Lamont-Doherty Earth Observatory, Columbia University, Palisades, NY, USA
[2]Department of Earth and Environmental Sciences, Columbia University, New York, NY, USA
[3]CRPG, CNRS, Université de Lorraine, 54 000 Nancy, France
[4]Lawrence Livermore National Laboratory, Livermore, CA USA
[5]Berkeley Geochronology Center, Berkeley CA USA

Correspondence to: Allie Balter-Kennedy (abalter@ldeo.columbia.edu)

Abstract. Here, we present cosmogenic [10]Be and [3]He data from Ferrar dolerite pyroxenes in surficial rock samples and a bedrock core from the McMurdo Dry Valleys, Antarctica, with the goal of refining the laboratory methods for extracting beryllium from pyroxene, further estimating the [10]Be production rate in pyroxene, and demonstrating the applicability of the [10]Be-[3]He in mafic rock. The ability to routinely measure cosmogenic [10]Be in pyroxene will open new opportunities for quantifying exposure durations and Earth surface processes in mafic rocks. We describe scalable laboratory methods for isolating beryllium from pyroxene, which includes a simple hydrofluoric acid leaching procedure for removing meteoric [10]Be, and the addition of a pH 8 precipitation step to reduce the cation load prior to ion exchange chromatography. [10]Be measurements in pyroxene from the surface samples have apparent [3]He exposure ages of 1–6 Ma. We estimate a spallation production rate for [10]Be in pyroxene, referenced to [3]He, of 3.6 ± 0.2 atoms g[-1] yr^{-1}. [10]Be and [3]He measurements in the bedrock core yield initial estimates for parameters associated with [10]Be and [3]He production by negative muon capture ($f_{10}^* = 0.00183$ and $f_3^* f_C f_D = 0.00337$).

Next, we demonstrate that the [10]Be-[3]He pair in pyroxene can be used to simultaneously resolve erosion rates and exposure ages, finding that the measured cosmogenic-nuclide concentrations in our surface samples are best explained by 2–8 Ma of exposure at erosion rates of 0–35 cm Myr[-1]. Finally, given the low [10]Be in our laboratory blanks (average of 5.7 x 10^{4} atoms), the reported measurement precision, and our estimated production rate, it should be possible to measure 2 g samples with [10]Be concentrations of 6 x 10^{4} atoms g[-1] and 1.5 x 10^{4} atoms g[-1] with 5 and 15% uncertainty, respectively. With this level of precision, Last Glacial Maximum to Late Holocene surfaces can now be dated with [10]Be in pyroxene. Application of [10]Be in pyroxene, alone or in combination with [3]He, will expand possibilities for investigating glacial histories and landscape change in mafic rock.

Short Summary. Cosmogenic nuclides like [10]Be are rare isotopes created in rocks exposed at the Earth's surface and can be used to understand glacier histories and landscape evolution. [10]Be is usually measured in the mineral quartz. Here, we show that [10]Be can be reliably measured in the mineral pyroxene. We use the measurements to determine

39   exposure ages and understand landscape processes in rocks from Antarctica that do not have quartz, expanding the
40   use of this method to new rock types.

41   **1 Introduction**

42   Cosmogenic nuclides are formed in minerals when rock is exposed to secondary cosmic radiation, and their
43   concentration at and near the Earth's surface hold information about exposure durations, burial time, and erosion rates
44   (e.g., Cerling, 1994; Kurz & Brook, 1994; Lal, 1991; Nishiizumi et al., 1991; Schaefer et al., 2022). Most simply, the
45   concentration of cosmogenic nuclides in rock serve as an exposure clock because they accumulate at known rates. It
46   is also possible to deconvolve complex exposure histories, involving exposure, burial, and rock erosion, by combining
47   measurements of multiple cosmogenic nuclides with different half-lives (e.g., Balco & Rovey, 2010; Granger, 2006;
48   Lal, 1991; Nishiizumi et al., 1991; Schaefer et al., 2016). In quartz-bearing (felsic) rocks, ^{21}Ne (stable), ^{10}Be ($t_{1/2} = 1.4$
49   Ma), ^{26}Al ($t_{1/2} = 0.7$ Ma), ^{14}C ($t_{1/2} = 5.7$ ka) are routinely measured, and different combinations of these nuclides can
50   be used to quantify geomorphic processes on 10^3–10^6 year timescales (e.g., Balco & Shuster, 2009; Hippe, 2017;
51   Young et al., 2021). ^{10}Be in quartz is the most commonly used nuclide-mineral pair because this mineral phase is
52   abundant at the Earth's surface, the production pathways for ^{10}Be in quartz are well understood, and advances in
53   beryllium extraction procedures and mass spectrometry have yielded measurement precision as low as ~2%.

54   In lithologies where quartz is absent, however, fewer cosmogenic nuclides are routinely measured. The stable
55   nuclide ^{3}He is the most widely used in mafic rocks because it is easily measured in several mineral phases, including
56   pyroxene and olivine. The radionuclide ^{36}Cl ($t_{1/2} = 0.3$ Ma) is also routinely measured in feldspar or whole rock, so
57   the ^{36}Cl/^{3}He pair could in principle be used to detect burial up to ~1.5 Ma. Prior work demonstrates that measuring
58   ^{10}Be in pyroxene and olivine is possible (Blard et al., 2008; Eaves et al., 2018; Ivy-Ochs et al., 1998; Nishiizumi et
59   al., 1990), which would extend the useful range for multi-nuclide studies in mafic rocks to >5 Ma in mafic rocks, ideal
60   for Miocene-to-Pleistocene timescales.

61   Several studies report ^{10}Be concentrations in pyroxene (Blard et al., 2008; Eaves et al., 2018; Ivy-Ochs et al.,
62   1998), but highlight challenges to measuring ^{10}Be in this mineral phase. First, the mineral composition of pyroxene
63   ($XYSi_2O_6$ where X is primarily divalent Ca, Na, Fe, Mg and Y is usually trivalent Al, Fe; Nespolo, 2020) is more
64   variable than quartz (SiO_2). In contrast to isolated beryllium from quartz, where Si is easily removed by evaporation
65   of SiF_6, separating beryllium from other cations after dissolution of pyroxenes requires highly selective column
66   chromatography. Second, early work on pyroxenes demonstrated difficulty in removing meteoric ^{10}Be,
67   atmospherically produced ^{10}Be scavenged by precipitation. In quartz, meteoric ^{10}Be is typically removed by repeated
68   leaching in hydrofluoric acid (HF; Kohl & Nishiizumi, 1992). Ivy-Ochs et al. (1998) demonstrated that ^{10}Be
69   concentrations in pyroxenes with exposure ages of ~10^6 yr did not stabilize after several rounds of HF leaching,
70   suggesting that meteoric ^{10}Be was present in clays and other weathering products built up within the pyroxene lattice.
71   In samples with 10^4-year exposure ages, Blard et al. (2008) successfully decontaminated pyroxene of meteoric ^{10}Be
72   by implementing a powdering step increase the surface area of pyroxene grains prior to leaching the samples in
73   hydroxylammonium-chloride, which removes iron oxides and releases meteoric ^{10}Be from the pyroxene grains. This
74   result was replicated by Eaves et al. (2018), but this procedure has yet to be tested on pyroxenes with exposure

75   durations longer than magnitude 10^4 years in which weathering products have had more time to accumulate within the

76   pyroxene lattice.

77   For cosmic-ray-produced nuclides to be useful in geologic applications, the production rate of these nuclides

78   at the Earth's surface and with depth in rock must be known. ^{10}Be and ^{3}He, like most cosmogenic nuclides, are

79   produced by spallation, fast muon interactions, and negative muon capture, production pathways that display different

80   dependencies (Dunai, 2010). Spallation reactions, induced by high energy (30 MeV–1GeV) neutrons comprise the

81   majority of production at the Earth's surface, but decrease rapidly with depth due to strong interaction with matter,

82   with a latitude-dependent attenuation length in rock of 140–160 g cm^{-2} (Gosse & Phillips, 2001). Production by muons,

83   which interact weakly with matter, comprise up to ~2% of production at the surface but surpass spallation production

84   below the upper several meters of rock. For this weak interaction production pathway, ^{10}Be and ^{3}He are primarily

85   produced by negative muon capture in the upper rock column, while fast muon reactions attenuate more slowly with

86   depth from the surface (Balco, 2017; Heisinger et al., 2002a; Heisinger et al., 2002b; Lal, 1987; Larsen et al., 2021;

87   Nesterenok & Yakubovich, 2016).

88   The spallation production rate of ^{3}He in pyroxene is well known (Borchers et al., 2016). Eaves et al. (2018)

89   used cross-calibration between ^{10}Be and ^{3}He (combining new data with those of Blard et al., 2008 and Nishiizumi,

90   1990) to estimate a spallation ^{10}Be production rate in pyroxene of 3.6 ± 0.8 atoms g^{-1} yr^{-1} (Eaves et al. also calibrated

91   a production rate for ^{10}Be in pyroxene of 3.2 ± 0.8 atoms g^{-1} yr^{-1} using independent age data). Theoretical studies

92   predict that cosmogenic ^{3}He is produced by muon interactions (Lal, 1987; Nesterenok & Yakubovich, 2016), and

93   recent ^{3}He measurements in a 300-m drill core from the Columbia River Basalt provide unambiguous empirical

94   evidence for muon production of ^{3}He at a total production rate of 0.23–0.45 atoms g^{-1} yr^{-1} at the Earth's surface at

95   high-latitude sea level (Larsen et al., 2021). Although parameters associated with muon production of ^{10}Be in quartz

96   are well known (Balco, 2017), muon production of ^{10}Be in pyroxene is not yet quantified.

97   Here, we describe progress in laboratory techniques for extracting beryllium from pyroxene, building upon

98   the previous work of Blard et al. (2008) and Eaves et al. (2018). We then use our new ^{10}Be and ^{3}He measurements in

99   pyroxenes from surface samples and a 1.7 m drill core from the McMurdo Dry Valleys, Antarctica, to further calibrate

100   the production rate of ^{10}Be by spallation, and present initial constraints on ^{10}Be and ^{3}He production by negative muon

101   capture. Finally, we use the sample set from the McMurdo Dry Valleys to demonstrate use of the ^{10}Be-^{3}He pair for

102   simultaneously estimating exposure ages and erosion rates in mafic rock.

103   **2 Geologic Setting**

104   The McMurdo Dry Valleys region of Antarctica is a 4,800 km^2 ice-free area in the northern Transantarctic

105   Mountains, bounded by the McMurdo Sound to the west and the East Antarctic Ice Sheet (EAIS) to the east. The

106   landscape is dissected by the large, east-west trending Taylor, Wright, and Victoria Valley systems that formerly held

107   outlet glaciers draining the EAIS to the Ross Sea, and are flanked by mountains, including The Asgard and Olympus

108   Ranges (Fig. 1). Geomorphic evidence suggests that this landscape had formed by the mid-Miocene and has since

109   been preserved in a cold, hyperarid climate (e.g., Sugden et al., 1995). This hypothesis is supported by extremely high

110   cosmogenic-nuclide concentrations throughout the region that are consistent with some of the lowest subaerial erosion

111   rates on Earth (0–30 cm Myr^{-1}; Bruno et al., 1997; Ivy-Ochs et al., 1995; Margerison et al., 2005; Schäfer et al., 1999;

112   Summerfield et al., 1999).

113   Large meltwater features, including channels, potholes, plunge pools, corrugated bedrock and megaripples,

114   found throughout the region are thought to have been carved by mid-Miocene outburst floods originating beneath an

115   expanded, wet-based EAIS (Denton & Sugden, 2005). ^{40}Ar/^{39}Ar ages on in situ volcanic ashes embedded in associated

116   sediments provide limiting ages on these features, suggesting that the major topographic features of the Dry Valleys

117   formed by ~15 Ma, and that the last glacial overriding event likely occurred by 14 Ma, and possibly by 14.8 Ma

118   (Denton et al., 1993). One prominent meltwater feature is the Labyrinth, a channel and pothole system carved into

119   Ferrar Dolerite bedrock located at the foot of Wright Upper Glacier, an outlet glacier of the EAIS. ^{39}Ar/^{40}Ar ages on

120   ashes from erosional surfaces within the Labyrinth date the last incision of this feature to ~14.5 Ma (Lewis et al.,

121   2006). In contrast, cosmogenic-nuclide concentrations in similar sandstone channel systems in Sessrumnir Valley,

122   Asgard Range, nearby to, although not directly adjacent to the Labyrinth, suggest that the Dry Valleys landscape has

123   been more dynamic since the mid-Miocene. There, paired ^{10}Be-^{21}Ne data reveal lower-than-expected cosmogenic

124   nuclide concentrations, which can be explained if these features were formed by wind erosion since ~14 Ma at erosion

125   rates of ~60–150 cm Myr^{-1}, or were incised by subglacial flooding during a later episode of ice cover, such as during

126   the Pliocene (Middleton et al., 2012). Overall, channel and pothole features throughout the Dry Valleys, including the

127   Labyrinth, may have experienced ~14–15 Ma of exposure, although the mechanism and timing of formation for many

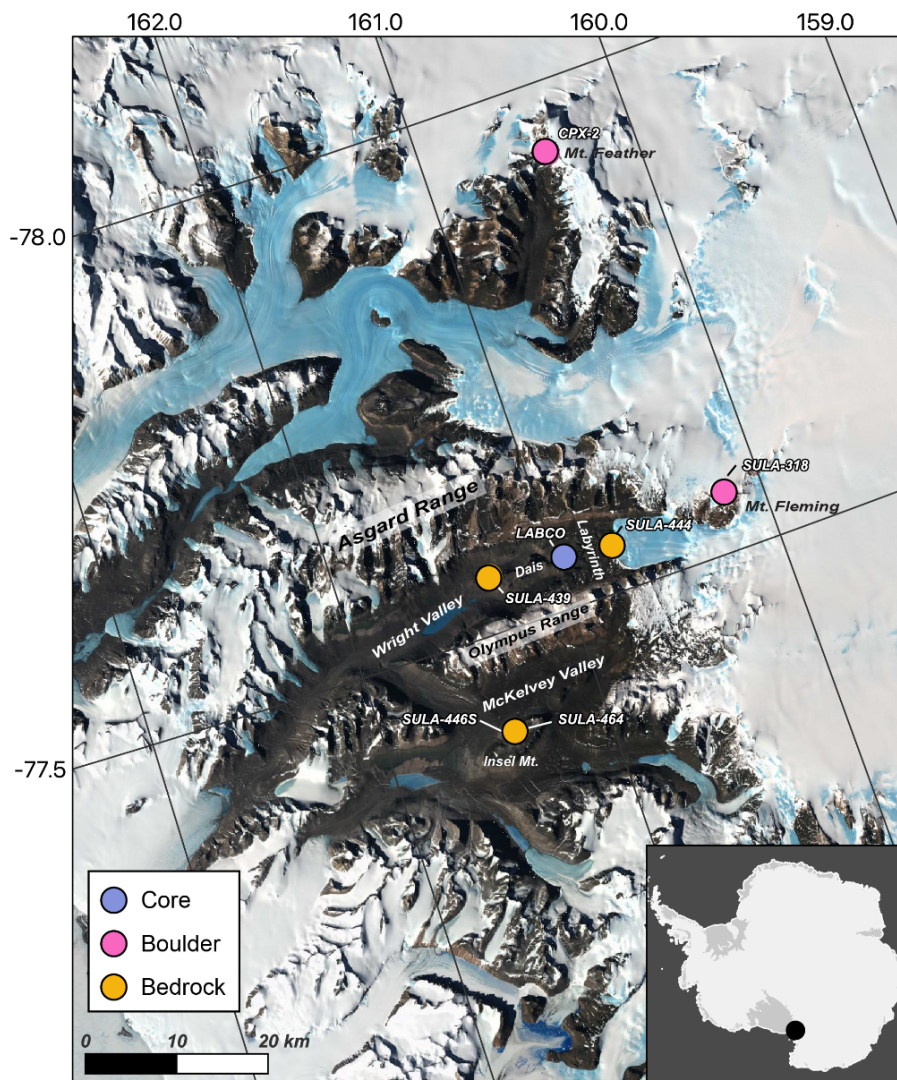128   of these features remain up for debate.

129

Figure 1: Map showing sample locations and places discussed in the text generated using Quantarctica Version 3 (Matsuoka et al., 2021). The base map employs the LIMA Landsat high-resolution virtual mosaic (Bindschadler et al., 2008).

130

131   In this study, we focus on Ferrar dolerite samples collected throughout the Dry Valleys region, originally

132   measured for cosmogenic noble gasses by Bruno et al. (1997) and Schaefer et al. (1999), that can be grouped into two

133   geomorphic environments: 1) boulders that are erosional remnants of the Sirius Group, located atop Mt. Fleming and

134   Mt. Feather at elevations >2000 m, in the Stable Upland Zone, which features the coldest and driest conditions in the

135 Dry Valleys (Lamp et al., 2017 and references therein); and 2) bedrock collected between ~850–1400 m from deeply

136 weathered platforms at Mt. Insel, the Dais, and the Labyrinth in the Inner Dry Valleys, somewhat closer to the Ross

137 Sea where conditions are slightly warmer and wetter (see Schäfer et al., 1999 and Bruno et al., 1997 for further detail;

138 Fig. 1). In addition to surface samples, we include results from a bedrock core collected from the Dais, an erosional

139 surface of the Labyrinth.

140

Table 1 - Location information for surface samples.

Sample ID	Location	Sample type	Latitude[3] (DD)	Longitude[3] (DD)	Elevation (m)	Thickness (cm)	Shielding
318[1]	Mt. Fleming	boulder	-77.56	160.17	2140	1.5	1
439	Dais	bedrock	-77.56	161.31	870	1.5	1
446S	Mt. Insel	bedrock	-77.40	161.43	1410 [4]	1.5	1
464	Mt. Insel	bedrock	-77.40	161.42	1395 [4]	1.5	1
NXP 93*52[2]	Mt. Feather	boulder	-77.93	160.42	2555	1.5	1
444	Labyrinth	bedrock	-77.55	160.74	1145	1.5	1
Labyrinth Core	Labyrinth	core	-77.54976	160.9578	990.2	1	1

[1]Sample listed as Flem94-18 in Bruno et al. (1997), and is the only sample listed here included in that publication.

[2]Sample NXP 93*52 is derived from the same sample as the reference material CRONUS-P (Schaefer et al., 2016).

[3]Latitudes and longitudes for surface samples are approximated from the United States Geological Survey (1988) Taylor Glacier Map, as latitudes and longitudes were not reported in the original publications associated with these samples (Bruno et al., 1997; Schäfer et al., 1999). See Supplementary Information for location approximation methods.

[4]Sample elevations used here are 120 m lower than reported in Schäfer et al. (1999) due to inaccuracies with pressure-based altimeter/early handheld GPS. See Supplementary Information.

141 **3 Methods**

142 **3.1 Field methods**

143 We present results from surficial rock samples and a bedrock core. The surficial rock samples are six Ferrar

144 Dolerites collected from the upper few centimeters of rock in the Dry Valleys in the early- to mid-1990s and described

145 by Schäfer et al. (1999) and Bruno et al. (1997) (2 boulders and 4 bedrock surfaces; Table 1). We redetermined surface

146 sample locations and elevations by reference to the U.S. Geological Survey Taylor Glacier topographic map (1988),

147 because of some inaccuracies with the location information in those original publications (see Table 1; Supplementary

148 Information). The Labyrinth dolerite bedrock core was collected by a group led by John Stone of the University of

149 Washington in austral summer 2009 as part of the CRONUS-Earth project (Table 1; Fig. 1; Sect. 2). The coring site

150 was chosen because erosion rates appeared to be low (10–20 cm Myr^{-1}) and previous work suggests that the site

151   has been exposed for the last ~14 Ma (Lewis et al., 2006; Sect. 2). Importantly, below 18 cm depth, there was a

152   discrepancy between the drillers' measurements on the core barrel and the recovered core length by 1–4 cm. No

153   material was lost between 18–167 cm, but we account for this discrepancy by adjusting the absolute sample depths

154   below 18 cm in a model fitting exercise described in Sect. 5.1.1. The core was split into sections at the University of

155   Washington and measured for rock density, which averages 2.94 g cm^{-3} throughout the core. Sections of the core were

156   then sent to several institutions, including Lamont-Doherty Earth Observatory (LDEO), Berkeley Geochronology

157   Center (BGC), and Le Centre de Recherches Pétrographiques et Géochimiques (CRPG), for cosmogenic-nuclide

158   analysis.

159   **3.2 Cosmogenic-nuclide measurements**

160   **3.2.1 Mineral separation and decontamination**

161   Pyroxene separated from the surface samples was prepared at LDEO, and samples from the Labyrinth core

162   were prepared at LDEO, BGC, and CRPG. At LDEO, samples were crushed and sieved to a grain size at which we

163   observed mostly mono-mineralic grains (for the the fine-to-medium grained samples here, we used the 32–125 μm

164   fraction) and then leached at room temperature in 10% H_3PO_4 overnight to remove iron oxides. Then light minerals

165   (mostly plagioclase) were removed using sodium polytungstate with a density of 3.0 g cm^{-3}. Next, samples were passed

166   through a magnetic separator and a hand magnet was used to remove magnetic minerals. To decontaminate the

167   pyroxene grains of meteoric ^{10}Be, samples were leached in a 1%HF/1%HNO$_3$ solution twice at room temperature for

168   5–6 hours, then a third time overnight, rinsing samples thoroughly between each round of leaching (Bromley et al.,

169   2014; Kohl & Nishiizumi, 1992). Overall, we targeted ~30% sample mass loss after leaching. To confirm sufficient

170   removal of meteoric ^{10}Be, five leaching rounds were performed on sample 444 and the ^{10}Be concentration was

171   measured on a split taken after each round. After two rounds of leaching, with ~25% sample loss, ^{10}Be concentrations

172   in sample 444 remain consistent within measurement error, suggesting that this leaching method was sufficient for

173   removing meteoric ^{10}Be (Fig. 2). Pyroxenes separated at LDEO are referred to as "LDEO-prepared."

Table 2 – Cosmogenic-nuclide concentrations, apparent exposure ages, and apparent erosion rates for surface samples.

Sample ID	Location	Measured [3He] (atoms g⁻¹)	[3He] normalized to CRONUS-P (atoms g⁻¹)	[3He] error (atoms g⁻¹)	Measured [10Be] (atoms g⁻¹)	[10Be] Error (atoms g⁻¹)	Apparent 3He exposure age (years)	Apparent exposure 3He age error (years)	Apparent 10Be exposure age[4] (years)	Apparent 10Be exposure age error (years)	10Be/3He age ratio[5]	Apparent 3He erosion rate (cm/Myr)	Apparent 3He erosion rate error (cm/Myr)
318[1]	Mt. Fleming	6.09E+09	5.87E+09	1.50E+08	5.06E+07	1.21E+06	6.25E+06	1.54E+05	4.39E+06	3.82E+05	0.70	8.7	0.2
439	Dais	9.20E+08	8.86E+08	2.00E+07	1.55E+07	3.72E+05	2.58E+06	5.62E+04	2.71E+06	1.38E+05	1.05	21.1	0.5
446S	Mt. Insel	3.08E+09	2.97E+09	8.00E+07	2.84E+07	6.80E+05	5.47E+06	1.42E+05	3.97E+06	3.00E+05	0.72	10.0	0.3
464	Mt. Insel	2.78E+09	2.68E+09	7.00E+07	2.75E+07	6.57E+05	5.00E+06	1.26E+05	3.73E+06	2.61E+05	0.75	10.9	0.3
NXP 93*52[2]	Mt. Feather	5.21E+09	5.02E+09	2.50E+08	6.46E+07	1.54E+06	4.04E+06	1.94E+05	3.91E+06	2.89E+05	0.97	13.5	0.7
444	Labyrinth	5.20E+08	5.01E+08	2.00E+07	1.02E+07	2.46E+05	1.15E+06	4.42E+04	9.72E+05	3.02E+04	0.85	47.3	0.2
Labyrinth Core[3]	Labyrinth	4.54E+08	4.77E+08	9.23E+06	-	-	1.24E+06	2.53E+04	8.25E+05	1.53E+04	0.66	43.8	0.9

[1] Sample listed as Flem94-18 in Bruno et al. (1997), and is the only sample listed here included in that publication.

[2] Sample NXP 93*52 is derived from the same sample as the reference material CRONUS-P (Schaefer et al., 2016).

[3] He-3 concentrations listed here are for the surface sample only in which 10Be was not measured. See Table 3 for subsurface sample results. To calculate the 10Be surface exposure age, a surface 10Be concentration was approximated by fitting an exponential curve to the subsurface 10Be data.

[4] Apparent 10Be exposure ages calculated using the 10Be in pyroxene spallation production rate from Eaves et al. (2018) of 3.6 ± 0.8 atoms g⁻¹ yr⁻¹ and v3 of the online exposure age calculator.

[5] Ratio close to 1 indicates 10Be and 3He ages are concordant.

175
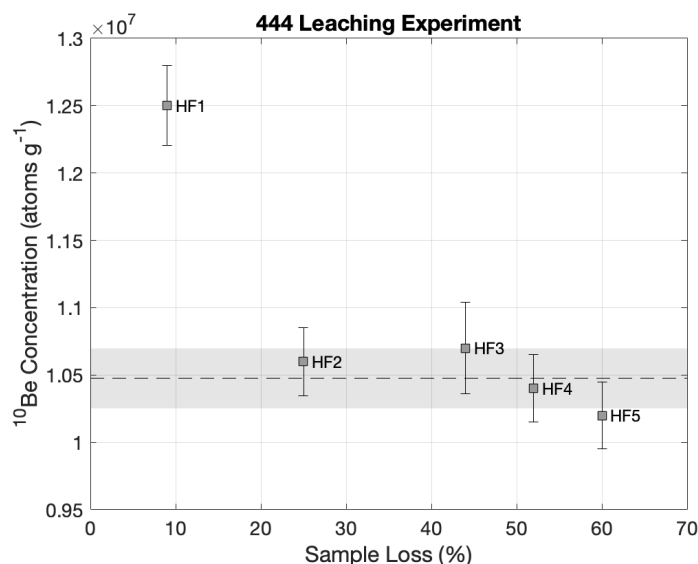
Figure 2: [10]Be concentrations measured after each of five progressive leaches on pyroxenes from sample 444. Total sample material loss ranges from 9% in Leach 1 to 60% in Leach 5. The dashed black line shows the average [10]Be concentration of HF2–HF5, and the shaded box shows the standard deviation of those [10]Be concentrations. The HF2–HF5 concentrations overlap within uncertainty, suggesting that 20–25% sample loss is enough to sufficiently remove meteoric [10]Be from old Ferrar dolerite samples.

Pyroxene preparation procedures at BGC and CRPG, where pyroxenes were measured only for [3]He, was similar to those at LDEO, but did not include an HF leaching step. BGC received from the University of Washington a heavy mineral concentrate prepared by crushing, sieving to extract grains in the 125-250 micron size range, and heavy liquid separation at 2.9 g cm^{-3}. This concentrate was then repeatedly passed through a magnetic separator at various settings to separate pure pyroxene from pyroxene-plagioclase aggregates (less magnetic) and oxide minerals (more magnetic). Remaining contaminant grains were then removed by hand-picking under a microscope. At CRPG, samples were crushed and sieved to 150–800 μm, plagioclase was removed by heavy liquid separation at a density of 3.3 g cm^{-3}, and then samples underwent magnetic separation and handpicking to improve the selection of pure pyroxenes.

3.2.2 Cosmogenic [3]He analyses

[3]He concentrations in the Labyrinth bedrock core samples were measured at LDEO, BGC, and CRPG. For quality control, internal comparability, and interlaboratory calibration, we also measured helium isotopes in the CRONUS-P pyroxene reference material, which is derived from the NXP 93*52 surface sample (Blard et al., 2015; Schaefer et al., 2016; Table 2). For all samples, we normalize the measured [3]He concentrations to the accepted CRONUS-P value [(5.02 ± 0.05) x 10^9; Tables 1 and 2; Blard, 2021; Blard et al., 2015]. At all laboratories, relative measurement uncertainties for the Labyrinth core samples increased with depth owing to the decreasing [3]He concentrations, ranging from 2% in the uppermost sample to 4% in the lowermost sample.

199   At LDEO, we measured helium isotopes in eight LDEO-prepared Labyrinth core samples. We extracted

200   helium in two subsequent heating steps, 5 minutes at ~900°C and 15 minutes at 1350°C in a resistance-heated double

201   vacuum furnace. Following purification with a charcoal-filled lN2-cooled U-trap and SEAS getter, the gas was cryo-

202   trapped at 14°C. The helium fraction was released at 45°C and ^{3}He and ^{4}He were measured by peak jumping in a MAP

203   215-50 (e.g., Winckler et al., 2005). Spectrometer sensitivity was determined using a Yellowstone helium standard

204   (Murdering Mudpots) with a ^{3}He/^{4}He ratio of 16.45R_a (where R_a = (^{3}He/^{4}He)$_{air}$ = 1.384 x 10^{-6}). At LDEO, the mean

205   and standard deviation of the ^{3}He concentrations measured in the CRONUS-P reference material at the same time as

206   the Labyrinth core samples was (5.16 ± 0.19) x 10^9 atoms g^{-1} (n = 5; coefficient of variance (CV) = 4%).

207   At CRPG, 34 measurements were made on 15 CRPG-prepared Labyrinth core samples and 5 measurements

208   were made on 5 BGC-prepared Labyrinth core samples. Sample extraction was realized by complete fusion at 1500°C

209   in our home-design extraction furnace (Blard, 2021; Zimmermann et al., 2018). Typical blanks were (2.1 ± 1.4) x 10^{-}

210   ^{20} mol of ^{3}He and (1.9 ± 0.1) x 10^{-15} mol of ^{4}He. Extracted gas was then purified, cryofocused at 8K and released at

211   75K in a GV-Split Flight Tube mass spectrometer to measure ^{3}He and ^{4}He abundances. The mass spectrometer

212   sensitivity was established with the helium standard of Matsuda et al. (2002). At CRPG, the CRONUS-P ^{3}He

213   concentrations, measured between March and April 2019 were (5.04 ± 0.12) x 10^9 atoms g^{-1} (n = 8; CV = 2%).

214   At BGC, 32 measurements were made on 14 BGC-prepared Labyrinth core samples and 5 measurements

215   were made on 3 CRPG-prepared Labyrinth core samples for the purpose of interlaboratory comparison. Cosmogenic

216   ^{3}He measurements at BGC employ a laser "microfurnace" extraction system coupled to a MAP-215 mass spectrometer

217   and are described in detail in Balter-Kennedy et al. (2020). At BGC, ^{3}He concentrations measured in CRONUS-P at

218   the same time as the Labyrinth core samples were (4.78 ± 0.08) x 10^9 atoms g^{-1} (n = 5; CV = 2%).

219   For the surface samples, we used existing ^{3}He measurements made at LDEO, described in Schaefer et al.

220   (2006; Table 2). Although not used in our calculations, earlier ^{3}He measurements were made and published from these

221   samples at ETH Zurich and Potsdam (Niedermann et al., 2007; Schäfer et al., 1999). ^{3}He measurement uncertainties

222   for the surface samples range from 2–3%. The ^{3}He concentration in sample NXP 93*52, measured alongside the other

223   surface samples and the same sample from which the CRONUS-P reference material was derived, is (5.21 ± 0.25) x

224   10^9 atoms g^{-1} (Schaefer et al., 2006).

3.2.3 Cosmogenic ^{10}Be analyses

226   We extracted beryllium from clean pyroxene at LDEO using a procedure modified from the methods for

227   beryllium extraction from quartz (e.g., Bromley et al., 2014; Kohl & Nishiizumi, 1992; Schaefer et al., 2009;

228   https://www.ldeo.columbia.edu/res/pi/tcn/Lamont_Cosmogenic_Nuclide_Lab/Chemistry_files/LDEO_Be_Chemistr

229   y_ver.4.pdf). The established procedure for extracting beryllium from quartz includes 1) addition of ^{9}Be carrier, 2)

230   sample dissolution, 3) ion exchange chromatography using anion and then cation exchange columns, 4) beryllium

231   precipitation, 5) combustion, and 6) preparation of AMS targets. Because of the high cation load present in pyroxenes,

232   Eaves et al. (2018) used small sample sizes (~2 g), and large resin volumes (20 mL) for cation exchange

233   chromatography. Nevertheless, they concluded that reduction of the cation load prior to ion chromatography using a

234   precipitation step would improve the extraction of beryllium from pyroxene. Here, we add a simple pH 8 precipitation

235   step to reduce the cation load in our samples prior to ion exchange chromatography. At pH 8, Be, Al and Fe precipitate

236   from solution as hydroxides, $Be(OH)_2$, $Al(OH)_3$ and $Fe(OH)_2$, while Ca and Mg remain in solution. We summarize

237   the LDEO methodology for pyroxene here.

238   For beryllium extraction from pure pyroxene separates we first weighed and spiked 100-200 mg of pyroxene

239   with ~180 μg of LDEO ^9Be carrier, containing very low ^{10}Be (Schaefer et al., 2009). The small sample sizes were

240   sufficient for these samples with high cosmogenic nuclide inventories and minimized the overall ion load. Samples

241   were digested in concentrated HF and HNO_3 and evaporated to dryness with 2–3 additions of perchloric acid to drive

242   off fluorides. The resulting residue was taken up in 1 mL 6M HCl, transferred to 15 ml centrifuge tubes, and diluted

243   with 10 mL of milli-Q water. NH_4OH was used to adjust the pH to 8, discarding the supernatant containing Ca, Mg,

244   Na and collecting the precipitate containing Be (and Al, Fe, Ti).

245   We isolated beryllium using ion chromatography methods described by (Kohl & Nishiizumi, 1992). Based

246   on the amount of Al in our samples (Table S3), we opted to use 2 mL of BioRad-50W X8 200–400# mesh resin for

247   cation exchange. Following cation exchange columns, the beryllium fraction was evaporated to dryness and then taken

248   up in 4 mL of 1% HNO_3, transferred to 15 mL centrifuge tubes, and diluted with 10 mL of milli-Q water. From this

249   solution, we precipitated $Be(OH)_2$ by adjusting the pH to 9 with NH_4OH. After pouring off the suprenate, this

250   precipitation step was repeated. We then performed three rinses of the precipitate with milli-Q water adjusted to pH

251   8. Several samples exceeded the exchange capacity of the cation exchange resin, allowing some Al to elute early with

252   Be. In these samples, the Be precipitates were noticeably larger than the blank, indicating that Al remained in the

253   sample. For these samples, we performed a second round of cation exchange chromatography, also with 2 mL of resin.

254   Following the second round of cation columns, the $Be(OH)_2$ precipitates for all samples were similar in size to the

255   blank, indicating that the second column step was successful in cleaning up the remainder of Al leftover after the first

256   round of columns.

257   The isolated beryllium was then combusted to form BeO, which we combined with Nb powder at an

258   approximate BeO:Nb ratio of 2:3 by volume, and loaded into stainless steel AMS cathodes. Packed targets were sent

259   to the Center for Accelerator Mass Spectrometry at Lawrence-Livermore National Laboratory for $^{10}Be/^9Be$

260   measurement relative to the 07KNSTD standard with a $^{10}Be/^9Be$ ratio of 2.85 x 10^{-12} (Nishiizumi et al., 2007).

261   Reported uncertainties in ^{10}Be measurements include 1σ uncertainty in the AMS measurement, uncertainty on the

262   blank correction, and error on the carrier concentration (1.5%), propagated in quadrature.

263         $^{10}Be/^9Be$ ratios in all fifteen samples range from 4 x 10^{-15} to 6 x 10^{-13}, with relative AMS uncertainties of <2–

264   8% (Table S1). $^{10}Be/^9Be$ ratios for all process blanks are magnitude 10^{-16}, equating to 3000–10500 atoms of ^{10}Be

265   (Table S2). Therefore, blank corrections for the surface samples are <0.5% and between 1–7.3% for the Labyrinth

266   core samples.

267   **3.3 Apparent exposure age and erosion rate calculations**

268   We calculate apparent exposure ages and erosion rates using Version 3 of the online calculator described by

269   Balco et al. (2008) and subsequently updated (http://hess.ess.washington.edu/math/v3/v3_age_in.html). All

270   calculations employ the 'St' scaling method of Stone (2000) and Lal (1991). To calculate the ^3He production rate, we

271   use the primary ^{3}He production rate dataset of (Borchers et al., 2016) in Version 3 of the online calculator (124 atoms

272   g^{-1} yr^{-1}; Balco et al., 2008; http://hess.ess.washington.edu/math/v3/v3_cal_in.html). Apparent exposure ages are

273   calculated assuming zero erosion and equate to a minimum age for the sample. Apparent erosion rates assume infinite

274   exposure time and represent a maximum erosion rate for the sample.

275   **4 Results**

276   The new ^{3}He and ^{10}Be data are shown in Tables 1 and 2, and in Figs. 3 and 4. Key features of these datasets

277   are summarized below.

278   **4.1 Cosmogenic ^{3}He concentrations**

279   Cosmogenic ^{3}He concentrations normalized using CRONUS-P in the surface samples range from 0.50–5.87

280   x 10^9 atoms g^{-1}, equating to apparent surface exposure ages of 1.2–6.3 Ma (Table 2). In the Labyrinth dolerite core,

281   CRONUS-P-normalized ^{3}He concentrations range from (4.75 ± 0.08) x 10^8 at the surface to (0.29 ± 0.01) x 10^8 at 164

282   cm depth (Table 3; Fig. 3). The ^{3}He concentration of the surface sample equates to an apparent exposure age of 1.2

283   Ma or an apparent erosion rate of 43.8 cm Myr^{-1} (Table 2). Measured cosmogenic ^{3}He concentrations in the Labyrinth

284   core differ slightly among the three labs (Table 3) but normalizing to CRONUS-P brings the BGC-prepared and

285   LDEO-prepared concentrations into agreement within ~5% (Fig. 3). The CRONUS-P-normalized ^{3}He concentrations

286   for the CRPG-prepared samples, however, are systematically lower than the LDEO-prepared and BGC-prepared

287   samples (up to ~15% lower). This is true also for the CRPG-prepared samples that were measured at BGC. Higher-

288   than-expected Al concentrations measured by ICP-OES in the CRPG-prepared pyroxene (Tables S4 and S5), along

289   with photos of those separated pyroxene grains, suggest that plagioclase may still be present in these samples. To

290   confirm, we applied a mixing model to determine the percentage of pyroxene, plagioclase, and magnetite (a common

291   accessory mineral in Ferrar Dolerite) in the CRPG samples and found that the CRPG-prepared samples contain >10%

292   plagioclase (see Supplemental Information). The contamination by plagioclase is the likely reason for the lower ^{3}He

293   concentrations in the CRPG-prepared samples because ^{3}He is poorly retained in that mineral phase (Cerling, 1990),

294   so this contamination by plagioclase is the likely reason for the lower. Therefore, we exclude the ^{3}He measurements

295   on the CRPG-prepared pyroxenes from further discussion. Notably, the ^{4}He concentrations were systematically higher

296   in the non-etched BGC-prepared (and CRPG-prepared) samples than in the LDEO-prepared samples, which were HF-

297   etched (Fig. S2).

Table 3 - Cosmogenic-nuclide concentrations for the Labyrinth core.

Sample ID	Average depth (cm)	Aliquot	Measured [³He] (atoms g⁻¹)	[³He] normalized to CRONUS-P (atoms g⁻¹)	[³He] error (atoms g⁻¹)	[⁴He] (atoms g⁻¹)	[⁴He] error (atoms g⁻¹)	Measured [¹⁰Be] (atoms g⁻¹)	[¹⁰Be] error (atoms g⁻¹)	Lab for pyroxene separation	Lab for ³He analysis
LABCO-01	24.5	a	3.31E+08	3.22E+08	6.18E+06	5.90E+13	8.44E+11	5.21E+06	1.45E+05	LDEO	LDEO
LABCO-02	34.5	a	2.66E+08	2.59E+08	5.24E+06	6.58E+13	9.36E+11	4.39E+06	1.17E+05	LDEO	LDEO
LABCO-03	49.5	a	2.04E+08	1.98E+08	5.26E+06	7.45E+13	2.41E+12	3.28E+06	1.06E+05	LDEO	LDEO
LABCO-04	59.5	a	1.73E+08	1.68E+08	4.37E+06	5.93E+13	2.08E+12	2.60E+06	8.11E+04	LDEO	LDEO
LABCO-05	84	a	9.96E+07	9.69E+07	2.34E+06	5.56E+13	7.95E+11	1.57E+06	5.90E+04	LDEO	LDEO
LABCO-06 (#1)	104	a	6.74E+07	6.56E+07	2.07E+06	3.85E+13	2.04E+12	9.01E+05	4.59E+04	LDEO	LDEO
LABCO-06 (#2)	104	a	-	-	-	-	-	1.11E+06	4.32E+04	LDEO	LDEO
LABCO-07	125	a	-	-	-	-	-	7.78E+05	4.22E+04	LDEO	LDEO
LABCO-08	144	a	4.11E+07	4.00E+07	1.47E+06	4.81E+13	2.11E+12	5.25E+05	3.54E+04	LDEO	LDEO
LABCO-09	164	a	3.00E+07	2.92E+07	1.24E+06	4.12E+13	2.01E+12	4.32E+05	3.86E+04	LDEO	LDEO
DOL_3	2.5	a	3.85E+08	3.83E+08	1.02E+07	1.47E+14	1.11E+12	-	-	CRPG	CRPG
DOL_3_bis	2.5	b	4.14E+08	4.12E+08	1.11E+07	1.28E+14	9.85E+11	-	-	CRPG	CRPG
DOL_3_a	2.5	c	3.99E+08	3.97E+08	1.36E+07	2.27E+14	1.81E+12	-	-	CRPG	CRPG
DOL_3_a	2.5	a	3.88E+08	4.07E+08	1.56E+07	1.83E+14	6.42E+12	-	-	CRPG	BGC
DOL_4	3.5	a	3.89E+08	3.87E+08	1.01E+07	1.88E+14	1.39E+12	-	-	CRPG	CRPG
DOL_4_b	3.5	b	3.76E+08	3.74E+08	1.38E+07	2.08E+14	1.65E+12	-	-	CRPG	CRPG
DOL_5	4.5	a	3.65E+08	3.64E+08	9.32E+06	3.07E+14	1.18E+12	-	-	CRPG	CRPG
DOL_5_a	4.5	b	3.41E+08	3.39E+08	1.23E+07	2.72E+14	2.10E+12	-	-	CRPG	CRPG
DOL_5_b	4.5	c	3.99E+08	3.97E+08	1.27E+07	1.34E+14	1.16E+12	-	-	CRPG	CRPG
DOL_6_a	5.5	a	3.35E+08	3.33E+08	1.17E+07	1.50E+14	1.28E+12	-	-	CRPG	CRPG
DOL_6_b	5.5	b	3.48E+08	3.47E+08	1.22E+07	2.14E+14	1.78E+12	-	-	CRPG	CRPG
DOL_7	6.5	a	3.40E+08	3.38E+08	9.19E+06	1.30E+14	9.94E+11	-	-	CRPG	CRPG

Table 3 cont'd.

Sample ID	Average depth (cm)	Aliquot	Measured [³He] (atoms g⁻¹)	[³He] normalized to CRONUS-P (atoms g⁻¹)	[³He] error (atoms g⁻¹)	[⁴He] (atoms g⁻¹)	[⁴He] error (atoms g⁻¹)	Measured [¹⁰Be] (atoms g⁻¹)	[¹⁰Be] error (atoms g⁻¹)	Lab for pyroxene separation	Lab for ³He analysis
DOL_7_a	6.5	b	3.45E+08	3.43E+08	1.25E+07	1.57E+14	1.33E+12	-	-	CRPG	CRPG
DOL_7_b	6.5	c	3.33E+08	3.32E+08	1.26E+07	1.36E+14	1.20E+12	-	-	CRPG	CRPG
DOL_9_a	8.5	a	3.49E+08	3.48E+08	1.16E+07	2.33E+14	1.83E+12	-	-	CRPG	CRPG
DOL_9_b	8.5	b	3.25E+08	3.23E+08	1.16E+07	1.97E+14	1.59E+12	-	-	CRPG	CRPG
DOL_10	9.5	a	3.27E+08	3.26E+08	9.45E+06	1.55E+14	1.17E+12	-	-	CRPG	CRPG
DOL_10_bis	9.5	b	3.32E+08	3.30E+08	9.18E+06	1.22E+14	9.38E+11	-	-	CRPG	CRPG
DOL_11_a	10.5	a	2.72E+08	2.71E+08	1.12E+07	1.75E+14	1.45E+12	-	-	CRPG	CRPG
DOL_11_b	10.5	b	2.71E+08	2.69E+08	1.08E+07	1.55E+14	1.30E+12	-	-	CRPG	CRPG
DOL_13	23.5	a	2.50E+08	2.49E+08	7.38E+06	1.77E+14	1.31E+12	-	-	CRPG	CRPG
DOL_13_b	23.5	b	2.56E+08	2.54E+08	9.83E+06	1.69E+14	1.40E+12	-	-	CRPG	CRPG
CRPG-DOL13a	23.5	a	2.65E+08	2.79E+08	1.08E+07	1.83E+14	6.40E+12	-	-	CRPG	BGC
CRPG-DOL13b	23.5	b	2.59E+08	2.72E+08	1.03E+07	1.74E+14	6.05E+12	-	-	CRPG	BGC
CRPG-DOL13c	23.5	c	2.55E+08	2.68E+08	1.06E+07	2.06E+14	7.22E+12	-	-	CRPG	BGC
DOL_14	33.5	a	1.82E+08	1.81E+08	6.12E+06	2.09E+14	1.53E+12	-	-	CRPG	CRPG
DOL_14_bis	33.5	b	2.05E+08	2.04E+08	6.53E+06	1.58E+14	1.19E+12	-	-	CRPG	CRPG
DOL_14_b	33.5	c	2.20E+08	2.19E+08	8.87E+06	2.13E+14	1.68E+12	-	-	CRPG	CRPG
DOL_16	58.5	a	1.31E+08	1.31E+08	4.83E+06	1.48E+14	1.11E+12	-	-	CRPG	CRPG
DOL_16_bis	58.5	b	1.25E+08	1.24E+08	4.92E+06	1.83E+14	1.36E+12	-	-	CRPG	CRPG
DOL_16_c	58.5	c	1.29E+08	1.29E+08	7.33E+06	1.84E+14	1.51E+12	-	-	CRPG	CRPG
DOL_17	82	a	8.96E+07	8.92E+07	3.85E+06	1.94E+14	1.43E+12	-	-	CRPG	CRPG
DOL_17_bis	82	b	9.03E+07	8.99E+07	3.95E+06	1.68E+14	1.25E+12	-	-	CRPG	CRPG
CRPG-DOL17a	82	a	9.28E+07	9.75E+07	5.79E+06	1.96E+14	6.90E+12	-	-	CRPG	BGC
DOL_18	102	a	5.51E+07	5.49E+07	3.20E+06	1.80E+14	1.33E+12	-	-	CRPG	CRPG

Table 3 cont'd.

Sample ID	Average depth (cm)	Aliquot	Measured [³He] (atoms g⁻¹)	[³He] normalized to CRONUS-P (atoms g⁻¹)	[³He] error (atoms g⁻¹)	[⁴He] (atoms g⁻¹)	[⁴He] error (atoms g⁻¹)	Measured [¹⁰Be] (atoms g⁻¹)	[¹⁰Be] error (atoms g⁻¹)	Lab for pyroxene separation	Lab for ³He analysis
DOL_18_bis	102	b	5.34E+07	5.32E+07	3.27E+06	2.13E+14	1.56E+12	-	-	CRPG	CRPG
DOL_20	142	a	3.92E+07	3.90E+07	2.69E+06	1.48E+14	1.12E+12	-	-	CRPG	CRPG
DOL_20_bis	142	b	3.55E+07	3.54E+07	2.65E+06	1.27E+14	9.78E+11	-	-	CRPG	CRPG
DOL_21	162	a	3.01E+07	3.00E+07	2.57E+06	2.45E+14	9.88E+11	-	-	CRPG	CRPG
LABCO-0-1-Px	0.5	b	4.52E+08	4.75E+08	7.81E+06	1.55E+14	1.35E+12	-	-	BGC	BGC
LABCO-0-1-Px	0.5	c	4.45E+08	4.67E+08	5.08E+06	1.60E+14	4.64E+11	-	-	BGC	BGC
LABCO-0-1-Px	0.5	d	4.64E+08	4.87E+08	6.08E+06	1.99E+14	5.78E+11	-	-	BGC	BGC
LABCO-0-1-Px	0.5	a	4.95E+08	4.93E+08	1.63E+07	1.48E+14	5.45E+11	-	-	BGC	CRPG
LABCO-1-2-Px	1.5	b	4.41E+08	4.63E+08	7.45E+06	2.00E+14	1.52E+12	-	-	BGC	BGC
LABCO-1-2-Px	1.5	c	4.45E+08	4.68E+08	5.30E+06	2.22E+14	6.53E+11	-	-	BGC	BGC
LABCO-1-2-Px	1.5	a	4.97E+08	4.95E+08	1.75E+07	2.36E+14	9.20E+12	-	-	BGC	CRPG
LABCO-4-5-Px	4.5	a	4.20E+08	4.41E+08	7.31E+06	2.06E+14	1.59E+12	-	-	BGC	BGC
LABCO-4-5-Px	4.5	b	4.23E+08	4.44E+08	5.49E+06	2.31E+14	9.02E+11	-	-	BGC	BGC
LABCO-4-5-Px	4.5	c	4.20E+08	4.41E+08	5.72E+06	2.10E+14	6.16E+11	-	-	BGC	BGC
LABCO-9-10-Px	9.5	b	3.86E+08	4.05E+08	6.83E+06	1.96E+14	1.49E+12	-	-	BGC	BGC
LABCO-9-10-Px	9.5	c	3.86E+08	4.06E+08	5.19E+06	1.89E+14	5.54E+11	-	-	BGC	BGC
LABCO-13-14-Px	13.5	a	3.46E+08	3.63E+08	6.27E+06	2.01E+14	1.54E+12	-	-	BGC	BGC
LABCO-13-14-Px	13.5	b	3.46E+08	3.64E+08	5.19E+06	1.85E+14	5.39E+11	-	-	BGC	BGC
LABCO-13-14-Px	13.5	c	3.54E+08	3.71E+08	4.92E+06	2.07E+14	6.03E+11	-	-	BGC	BGC
LABCO-20-21-Px	20.5	b	3.26E+08	3.43E+08	5.66E+06	1.89E+14	1.25E+12	-	-	BGC	BGC
LABCO-20-21-Px	20.5	c	3.14E+08	3.29E+08	5.65E+06	2.03E+14	1.67E+12	-	-	BGC	BGC
LABCO-20-21-Px	20.5	a	3.07E+08	3.06E+08	1.04E+07	1.97E+14	7.69E+12	-	-	BGC	CRPG
LABCO-30-31-Px	30.5	b	2.60E+08	2.73E+08	4.10E+06	2.25E+14	1.50E+12	-	-	BGC	BGC

Table 3 cont'd.

| Sample ID	Average depth (cm)	Aliquot	Measured [³He] (atoms g⁻¹)	[³He] normalized to CRONUS-P (atoms g⁻¹)	[³He] error (atoms g⁻¹)	[⁴He] (atoms g⁻¹)	[⁴He] error (atoms g⁻¹)	Measured [¹⁰Be] (atoms g⁻¹)	[¹⁰Be] error (atoms g⁻¹)	Lab for pyroxene separation	Lab for ³He analysis
LABCO-30-31-Px	30.5	c	2.65E+08	2.79E+08	4.84E+06	2.33E+14	1.80E+12	-	-	BGC	BGC
LABCO 30-31	30.5	a	2.84E+08	2.82E+08	1.00E+07	2.01E+14	7.84E+12	-	-	BGC	CRPG
LABCO-55-56-Px	55.5	b	1.62E+08	1.70E+08	3.13E+06	1.74E+14	1.33E+12	-	-	BGC	BGC
LABCO-55-56-Px	55.5	c	1.73E+08	1.81E+08	2.87E+06	1.77E+14	5.19E+11	-	-	BGC	BGC
LABCO 55-56	55.5	a	1.73E+08	1.73E+08	6.64E+06	1.74E+14	6.77E+12	-	-	BGC	CRPG
LABCO-75-77-Px	76	c	1.11E+08	1.16E+08	2.33E+06	2.34E+14	1.80E+12	-	-	BGC	BGC
LABCO-75-77-Px	76	d	1.16E+08	1.21E+08	2.61E+06	2.38E+14	7.03E+11	-	-	BGC	BGC
LABCO-75-77-Px	76	e	1.17E+08	1.23E+08	2.18E+06	2.11E+14	6.09E+11	-	-	BGC	BGC
LABCO-95-97-Px	96	a	8.72E+07	9.16E+07	2.09E+06	2.25E+14	1.74E+12	-	-	BGC	BGC
LABCO-95-97-Px	96	c	8.20E+07	8.61E+07	1.96E+06	2.22E+14	6.50E+11	-	-	BGC	BGC
LABCO-95-97-Px	96	d	8.09E+07	8.50E+07	1.95E+06	2.37E+14	6.92E+11	-	-	BGC	BGC
LABCO-116-118-Px	117	c	6.32E+07	6.63E+07	1.71E+06	2.64E+14	7.75E+11	-	-	BGC	BGC
LABCO-116-118-Px	117	d	6.28E+07	6.60E+07	1.76E+06	2.47E+14	7.18E+11	-	-	BGC	BGC
LABCO-135-137-Px	136	b	4.46E+07	4.68E+07	1.53E+06	2.02E+14	5.86E+11	-	-	BGC	BGC
LABCO-135-137-Px	136	c	4.72E+07	4.95E+07	2.03E+06	2.04E+14	5.97E+11	-	-	BGC	BGC
LABCO-135-137-Px	136	d	5.03E+07	5.28E+07	1.39E+06	2.04E+14	5.96E+11	-	-	BGC	BGC
LABCO-155-157-Px	156	c	3.66E+07	3.85E+07	1.60E+06	1.39E+14	4.28E+11	-	-	BGC	BGC
LABCO-155-157-Px	156	d	3.40E+07	3.57E+07	1.41E+06	1.48E+14	4.26E+11	-	-	BGC	BGC

299
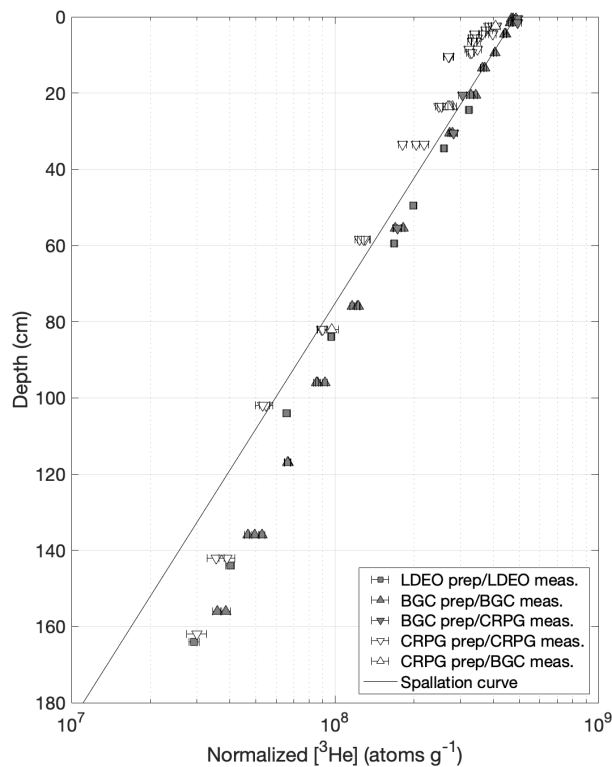
300
Figure 3: ³He concentrations from the Labyrinth core normalized to CRONUS-P. The CRPG-prepared samples were
excluded from the fitting procedure as described in Sect. 5.1.1. The solid black line is an exponential curve showing
spallation-produced ³He that was calculated using the surface ³He concentration and an attenuation length of 140 g cm⁻².
Below ~40 cm depth, the measured ³He concentrations are greater than the spallation curve, presumably due to production
by muons.
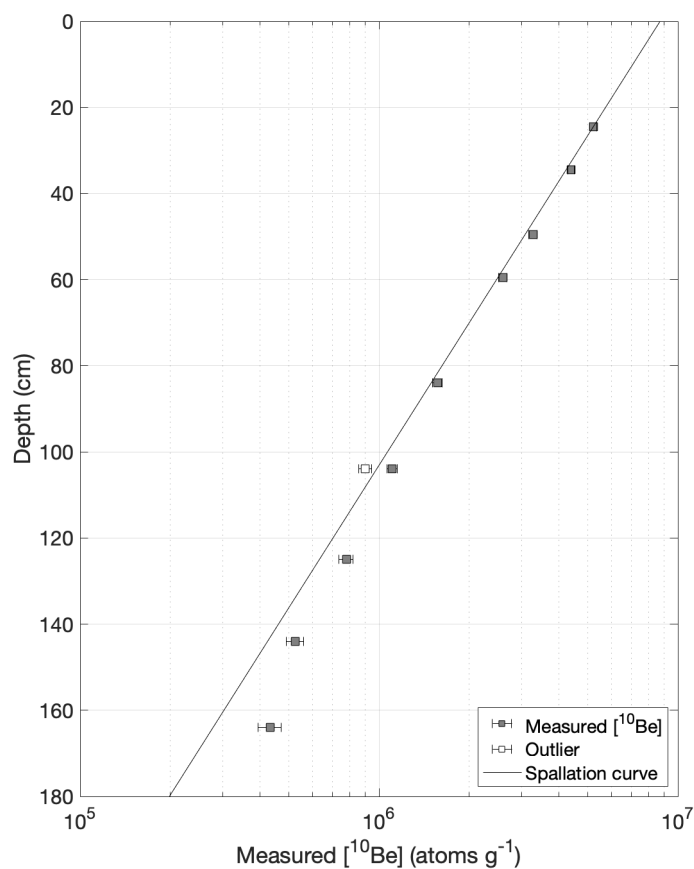
Figure 4: Measured [10]Be concentrations in pyroxenes from the Labyrinth core. All samples were prepared at LDEO and [10]Be/[9]Be ratios were measured at LLNL. The black line is an exponential curve showing the concentration of spallation-produced [10]Be, calculated using the measured [10]Be concentration at 24 cm depth and an attenuation length of 140 g cm^{-2}. Below ~100 cm depth, the measured [10]Be concentrations are greater than the spallation curve, indicating production by muons.

4.2 Cosmogenic [10]Be concentrations

[10]Be concentrations in the six surface samples range from 1.02–5.06 x 10^{7} atoms g[-1], with corresponding uncertainties of ~2%. Nine [10]Be concentrations between 24 and 164 cm depth in the Labyrinth bedrock core ranged from 5.21 x 10^{6} atoms g[-1] in the uppermost sample to 4.32 x 10^{5} atoms g[-1] in the lowermost sample (Table 3; Fig. 4). Our first [10]Be measurement of the Labyrinth core sample LABCO-06 clearly deviates from the rest of the depth profile, although the reasons for this are unknown. A second measurement of a re-processed split of LABCO-06, however, agrees with the rest of the [10]Be concentrations in the depth profile. Therefore, in the production rate calibration exercise described in Sect. 5.1.1, we use only the second measurement on LABCO-06. Total relative uncertainty (measurement

320 error, blank correction, and error on the carrier concentration, propagated in quadrature) increased from 3–9%
321 downcore.

322   Using a previously published production rate for ^{10}Be in pyroxene of 3.6 atoms g^{-1} yr^{-1} (Eaves et al., 2018),
323 the apparent ^{10}Be exposure ages of the surface samples range from 1.0–4.4 Ma, and the apparent ^{10}Be exposure age of
324 the Labyrinth core surface is ~830 ka (surface ^{10}Be concentration calculated by fitting an exponential curve to the ^{10}Be
325 data; therefore, surface ^{10}Be age for the Labyrinth core is approximate).

4.3 General observations

327   Here, we highlight several key features of our dataset that inform the production rate estimations in Sect. 5.1.
328 First, we observe that the apparent ^{3}He and ^{10}Be ages are discordant in surface samples 318, 444, 464, 446S and the
329 Labyrinth core surface (Table 2), suggesting that these samples have experienced complex exposure histories,
330 potentially involving subaerial erosion or burial (e.g., by ice or sediment), or both. The canonical interpretation is that
331 the geomorphic setting of these sample locations is consistent with a single period of exposure (Sect. 2), so a likely
332 reason for this discordance is subaerial erosion. This observation requires that we consider erosion when attempting
333 to estimate spallation and muon production rates in Sect. 5.1.

334   Figs. 3 and 4 show that the measured ^{10}Be and ^{3}He inventories in the Labyrinth core exceed those predicted
335 by a spallation curve below ~100 cm depth and ~40 cm depth, respectively, indicating that muon-produced ^{10}Be and
336 ^{3}He make up a significant portion of the measured concentrations below these depths. With this finding, we present
337 the first direct measurements of muon-produced ^{10}Be in pyroxene, and further confirm the importance of quantifying
338 muon production of ^{3}He (Larsen et al., 2021). At the depth range of the Labyrinth core, negative muon capture is the
339 primary muon production pathway. Therefore, we can use these data to estimate the negative muon cross-sections for
340 ^{3}He and ^{10}Be in pyroxene (Sect. 5.1.1).

5. Discussion

5.1 Production rate estimate

343   The goal of this section is to place limits on several key parameters associated with ^{10}Be and ^{3}He production
344 in pyroxene. Here, we use our Labyrinth core data to estimate parameters associated with spallation production of
345 ^{10}Be, and ^{10}Be and ^{3}He production by negative muon capture. In addition to the Labyrinth core, we use the surface
346 sample data to further refine the ^{10}Be spallation production rate in pyroxene. After estimating a production rate for
347 each sample, we combine our findings from the Labyrinth core and surface samples to arrive at a likely value for the
348 ^{10}Be spallation production rate.
349

5.1.1 Spallation and muon production in the Labyrinth core

351   We use the ^{10}Be and ^{3}He concentrations in pyroxenes from the Labyrinth core to estimate parameters
352 associated with ^{10}Be and ^{3}He production. To do so, we apply a forward model, adapted from Balco et al. (2019) to

353 include radioactive decay, that simulates the accumulation of cosmogenic ^{3}He and ^{10}Be by spallation and muon

354 production with depth. We then estimate several parameters related to ^{10}Be and ^{3}He production in pyroxene by fitting

355 the model to our measured ^{10}Be and ^{3}He concentrations.

356 Measured ^{3}He includes cosmogenic ^{3}He produced by neutron spallation, negative muon capture, fast muon

357 interactions, as well as some non-cosmogenic ^{3}He:

358 $$N_{3,m} = N_{3,sp} + N_{3,\mu^-} + N_{3,\mu f} + N_{3,non-cosmo} \text{ (Equation 1)}$$

359 $N_{3,m}$ (atoms g^{-1}) is the measured ^{3}He concentration, $N_{3,sp}$ (atoms g^{-1}) is ^{3}He produced by high-energy neutron

360 spallation, N_{3,μ^-} (atoms g^{-1}) is ^{3}He produced by negative muon capture, $N_{3,\mu f}$ (atoms g^{-1}) is ^{3}He produced by fast

361 muon reactions. $N_{3,non-cosmo}$ (atoms g^{-1}) is non-cosmogenic ^{3}He, which in Ferrar pyroxene is most likely produced

362 by neutron capture on Li via the reaction ^{6}Li(n, α)^{3}He (Ackert & Kurz, 2004; Andrews & Kay, 1982). In Ferrar

363 Dolerite, the total concentration of non-cosmogenic ^{3}He has been measured in samples that are shielded from the

364 cosmic-ray flux (Ackert, 2000; Kaplan et al., 2017; Margerison et al., 2005). Together, these measurements converge

365 on (3.3 ± 1.1) x 10^6 atom g^{-1} of non-cosmogenic ^{3}He throughout this lithology (see discussion in Balco, 2020).

366 In contrast, all the measured ^{10}Be is cosmogenic, produced by spallation and muon interactions:

367 $$N_{10,m} = N_{10,sp} + N_{10,\mu^-} + N_{10,\mu f} \text{ (Equation 2)}$$

368 Cosmogenic-nuclide production by high-energy neutron spallation decreases exponentially with mass depth

369 (Lal, 1991):

370 $$P_{i,sp}(z) = P_{i,sp}(0)e^{-\frac{z}{\Lambda_{sp}}} \text{ (Equation 3)}$$

371 where z is mass depth below the surface (g cm^{-2}), $P_{i,sp}(0)$ is the surface production rate of a given nuclide (atoms g^{-1}

372 yr^{-1}), and Λ_{sp} is the effective attenuation length for spallation production in mass depth (g cm^{-2}). Therefore, the

373 concentration of spallation-produced ^{3}He as a function of mass depth z is:

374 $$N_{3,sp}(z) = P_{3,sp,SLHL} * S_{St} \int_0^t e^{-\frac{z+\varepsilon\tau}{\Lambda_{sp}}} d\tau = \frac{P_{3,sp,SLHL} * S_{St} * e^{-\frac{z}{\Lambda_{sp}}} \Lambda_{sp}}{\varepsilon}(1 - e^{-\frac{\varepsilon t}{\Lambda_{sp}}}) \text{ (Equation 4)}$$

375 where $P_{3,sp,SLHL}$ is the reference production rate for ^{3}He at SLHL, S_{St} is the scaling factor using St scaling (Stone,

376 2000), t is the exposure duration (yr), ε is the surface erosion rate (g cm^{-2} yr^{-1}), and τ is a variable of integration. The

377 concentration of spallation-produced ^{10}Be, a radionuclide, as a function of mass depth z is:

378 $$N_{10,sp}(z) = P_{10,sp,SLHL} * S_{St} \int_0^t e^{-(\lambda_{10}+\frac{z+\varepsilon\tau}{\Lambda_{sp}})\tau} d\tau = \frac{P_{10,sp,SLHL} * S_{St} * e^{-\frac{z}{\Lambda_{sp}}}}{\lambda_{10} + \frac{\varepsilon}{\Lambda_{sp}}}(1 - e^{-(\lambda_{10} + \frac{\varepsilon}{\Lambda_{sp}})t}) \text{ (Equation 5)}$$

379 where $P_{10,sp,SLHL}$ is the SLHL reference production rate for ^{10}Be, λ_{10} is the decay constant for ^{10}Be (5.00 x 10^{-7} yr^{-1};

380 Chmeleff et al., 2010; Fink & Smith, 2007; Korschinek et al. 2010).

381 We adopt production by negative muon capture from Heisinger et al. (2002b) as:

382 $$N_{3,\mu^-} = f_3^* f_C f_D \int_0^t R_{\mu^-}(z + \varepsilon\tau) d\tau \text{ (Equation 6)}$$

383 $$N_{10,\mu^-} = f_{10}^* f_C f_D \int_0^t R_{\mu^-}(z + \varepsilon\tau)e^{-\lambda t} d\tau \text{ (Equation 7)}$$

384 where R_{μ^-} is the muon stopping rate, f_D is the probability that the negative muon does not decay in the K-shell before

385 capture by the nucleus, f_C is the chemical compound factor, and f_i^* is the probability that the nuclide of interest is

386   produced after negative muon capture by the target nucleus. For muon-produced ^{10}Be, the target nucleus is O, and we

387   aim to find the optimal value for f_{10}^*, which should be the same as the value of this parameter calibrated in quartz

388   (0.00191; Balco, 2017). For O in a Ferrar Dolerite pyroxene with composition En$_{34}$Fs$_{25}$Wo$_{42}$ (typical augite from a

389   medium-grained dolerite; Zavala et al., 2011), f_C = 0.520 (von Egidy & Hartmann, 1982). f_D is well known for O

390   (0.1828; Suzuki et al., 1987). In contrast, ^{3}He is produced in many negative muon capture reactions on a myriad of

391   targets (see Table 3 in Heisinger et al., 2002b). Therefore, we estimate the entire $f_3^* f_C f_D$ term, which represents the

392   overall probability that a negative muon produces ^{3}He. The $f_3^* f_C f_D$ term should be similar to 0.0045, which is the sum

393   of theoretical $f_3^* f_C f_D$ values for ^{3}He and ^{3}H producing reactions in standard rock (Nesterenok & Yakubovich, 2016).

394   Production by fast muon interactions is taken from Heisinger et al. (2002a) as:

395        $$N_{3,\mu f} = \sigma_{0,3} N_{pyx} \int_0^t \beta(z + \varepsilon\tau)\phi(z + \varepsilon\tau)\bar{E}^\alpha(z + \varepsilon\tau) \, d\tau \text{ (Equation 8)}$$

396        $$N_{10,\mu f} = \sigma_{0,10} N_{O,pyx} \int_0^t \beta(z + \varepsilon\tau)\phi(z + \varepsilon\tau)\bar{E}^\alpha(z + \varepsilon\tau)e^{-\lambda\tau} \, d\tau \text{ (Equation 9)}$$

397   Here, $\sigma_{0,i}$ is the cross-section for nuclide production by fast muons. Because the Labyrinth core does not extend to

398   depths dominated by fast-muon production, meaning that we cannot estimate the fast muon cross-sections with our

399   dataset, we apply fast muon cross-sections from other studies in our model. We take $\sigma_{0,10}$ to be the same as quartz

400   (0.280 μb; Balco, 2017), and $\sigma_{0,3}$ to be 6.01 μb, calculated by fitting Equation 8 to ^{3}He measurements in pyroxene

401   from a 300 m drill core of the Columbia River Basalt in Washington, USA (Larsen et al., 2021; see Supplementary

402   Information). N_{pyx} is the number of target atoms g^{-1} in standard basalt, assuming all elements are targets (2.74 x 10^{22}

403   atoms g^{-1}; average atomic mass 22) and $N_{O,pyx}$ is the number of atoms g^{-1} of O (1.57 x 10^{22} atoms g^{-1}; relevant for

404   ^{10}Be production) for a Ferrar Dolerite pyroxene with composition En$_{34}$Fs$_{25}$Wo$_{42}$ (Zavala et al., 2011). The remaining

405   terms in these equations yield the integrated muon flux at a given mass depth over time for a prescribed surface erosion

406   rate (see Heisinger et al., 2002a for symbol definitions). We evaluate Equations 13 and 14 using the "Model 1A"

407   MATLAB code of Balco (2017), with the parameter α set to 1 (see discussion in Borchers et al., 2016; Balco, 2017).

408   Together, Equations 6–14 comprise a forward model that we use to predict ^{3}He and ^{10}Be concentrations in

409   our core samples. We apply the known ^{3}He production rate calculated using the primary production dataset of Borchers

410   et al. (2016; see Sect 3.3), so our model has seven unknown parameters: the exposure duration, t; the surface erosion

411   rate, ε; the spallogenic ^{10}Be production rate at sea level high latitude (SLHL), $P_{10,sp,SLHL}$; the spallation attenuation

412   length, Λ_{sp}; the probability that negative muon capture creates ^{3}He and ^{10}Be, $f_3^* f_C f_D$ and f_{10}^* (since $f_C f_D$ are known

413   for ^{10}Be for the target O), respectively; and a variable to account for the core measurement offset below 18 cm depth

414   (see discussion in Sect. 3.1 regarding discrepancy between the drillers' measurements on the core barrel and the

415   recovered core length). We fit our model by minimizing the χ^2 misfit statistic, M:

416        $$M = \sum_j \left[\frac{N_{10,p,j} - N_{10,m,j}}{\sigma_{10,m,j}}\right]^2 + \sum_n \left[\frac{N_{3,p,n} - N_{3,m,n}}{\sqrt{\sigma_{3,m,n}^2 + \sigma_{3,non-cosmo}^2}}\right]^2$$

417   (Equation 10)

418   Where $N_{i,p}$ is the predicted cosmogenic-nuclide concentration, $N_{i,m}$ is the measured cosmogenic-nuclide

419   concentration, $\sigma_{i,m}$ is the associated measurement uncertainty, and $\sigma_{3,non-cosmo}$ is the uncertainty on the non-

420 cosmogenic ^{3}He concentration in Ferrar Dolerite. We impose the constraint that all parameters in this fitting exercise

421 must be greater than zero, except the variable accounting for the core measurement offset below 18 cm, which can

422 have any value.

423 The exposure history of a sample is important for determining parameters associated with cosmogenic-

424 nuclide production, as burial and erosion affect the accumulation of cosmogenic nuclides throughout the rock column.

425 Previous work suggests that the Labyrinth has been largely undisturbed since the mid-Miocene (Lewis et al., 2006;

426 Sect. 2). We thus assume that the Labyrinth core site has not experienced burial since the mid-Miocene. Erosion,

427 however, must be considered. Erosion advects rock from lower in the rock column towards the surface. In eroding

428 rock, therefore, the measured nuclide concentration at any given depth accumulated at a range of depths with varying

429 contributions from each of the muon production pathways. Therefore, the muon cross-sections and erosion rates cannot

430 be determined simultaneously, since infinite combinations of the two could yield the measured nuclide concentrations.

431 Because we cannot estimate all unknown parameters at the same time, we consider two end members that

432 capture the possible ranges for the production rate parameters given our measured ^{10}Be and ^{3}He concentrations. In the

433 first endmember scenario, we assume that the site has experienced a finite period of exposure, determined by the

434 apparent ^{3}He exposure age, and zero erosion. For the second endmember, we assume that the site has been exposed

435 for a much longer time than the apparent exposure age (several ^{10}Be half-lives) at a steady erosion rate. Based on those

436 endmembers we can place limits on the parameters associated with ^{10}Be and ^{3}He in pyroxene.

437 The steady erosion endmember affords a maximum value for spallation production of ^{10}Be. Solving Equation

438 5 for P$_{10,sp,SLHL}$ at the Earth's surface yields:

439
$$P_{10,sp,SLHL} = \frac{N_{10}(\lambda_{10} + \frac{\varepsilon}{\Lambda_{sp}})}{S_{St}(1 - e^{-(\lambda_{10} + \frac{\varepsilon}{\Lambda_{sp}})t})} \quad \text{(Equation 11)}$$

440

441 As $t \to \infty$, $P_{10,sp,SLHL} = N_{10}(\lambda_{10} + \frac{\varepsilon}{\Lambda_{sp}})/S_{St}$. Because ε must be between zero and ε_3 (the steady erosion rate from

442 the ^{3}He data; Sect. 4.1), $P_{10,sp,SLHL}$ must be between $(N_{10} * \lambda_{10})/S_{St}$ and $N_{10}(\lambda_{10} + \frac{\varepsilon_3}{\Lambda_{sp}})/S_{St}$.

443 The opposite is true for parameters associated with negative muon capture, where the steady erosion

444 endmember yields a minimum value for $f_3^* f_C f_D$ and f_{10}^* and the zero-erosion endmember yields a maximum. In

445 eroding rock, advection brings up cosmogenic nuclides produced at depths where fast muons comprise the majority

446 of production, meaning that, compared to the zero-erosion assumption, the steady-erosion assumption will yield

447 cosmogenic-nuclide concentrations with a higher proportion produced by fast muons and a smaller proportion

448 produced by negative muon capture. Because we prescribe values for the fast muon cross sections, the negative muon

449 cross section decreases in our steady erosion model to accommodate the fast-muon-produced inventory advecting up

450 from below. Therefore, the steady erosion endmember yields minimum values for $f_3^* f_C f_D$ and f_{10}^* and the zero-erosion

451 endmember will give maximum values for $f_3^* f_C f_D$ and f_{10}^*. In sum, the zero-erosion endmember will produce a lower

452 limit on the spallation production rate and an upper limit on parameters associated with nuclide

453   production by negative muon capture, and the steady erosion end member affords an upper limit on the spallation
454   production rate and a lower limit on the negative muon capture parameters. The optimal values for the production
455   parameters for each end member are listed in Table 4.
456

Table 4 - Optimal values for production parameters for ^{10}Be in pyroxene.

	Exposure age (Ma)	Erosion rate (cm Myr^{-1})	P$_{10,sp,SLHL}$ (atoms g^{-1} yr^{-1})	f_{10}* (dimensionless)	f_3*$f_C f_D$ (dimensionless)
Zero-erosion endmember	1.18	-	2.82	0.00534	0.05783
Steady-erosion endmember	-	41.1	3.36	0.00183	0.00337

457   *Zero-erosion endmember*
458   In the $\varepsilon = 0$ cm yr^{-1} endmember, there remain six unknown parameters: t, $P_{10,sp,SLHL}$, Λ_{sp}, $f_3^* f_C f_D$, and f_{10}^*,
459   and a variable to account for the core measurement offset below 18 cm. The minimum value of the χ^2 statistic, M, is
460   111 for 24 degrees of freedom (30 samples minus 6 fitting parameters), resulting in a reduced χ^2 value of 4.6. Because
461   the residuals do not appear systematic (Fig. 5), the likely reason for this high χ^2 value is errors unaccounted for in the
462   misfit statistic, such as the uncertainty associated with interlaboratory standardization.
463   The results of this fitting exercise are shown in Fig. 5. The best-fitting parameter values for the zero-erosion
464   case are $t = 1.18$ Ma, which agrees with the apparent ^{3}He age at the surface (1.24 Ma; Sect. 4.1). Optimal values for
465   spallation-related parameters in this model are $P_{10,sp,SLHL} = 2.82$ atoms g^{-1} yr^{-1} and $\Lambda_{sp} = 142$ g cm^{-2}. As discussed
466   above, $P_{10,sp,SLHL}$ should be a minimum in this end member, and the optimal value of 2.82 is indeed at the low end of
467   the $P_{10,sp,SLHL}$ confidence interval found in Eaves et al. (2018; 3.6 ± 0.8 atoms g^{-1} yr^{-1}). The fitted value for Λ_{sp} is close
468   to other estimates of the spallation attenuation length in Antarctica (140 g cm^{-2}; Gosse & Phillips, 2001), although the
469   attenuation length is expected to vary slightly for different nuclides and lithologies (Argento et al., 2015). The best-
470   fitting value for the measurement offset below 18 cm is 2.12 cm.
471   The optimal values for parameters related to negative muon capture in this scenario are $f_{10}^* = 0.00534$ and
472    $f_3^* f_C f_D = 0.05783$. Again, the zero-erosion end member should yield maximum constraints for these parameters. The
473   optimal value for f_{10}^* is the same magnitude as f_{10}^* for quartz (0.00191; Balco, 2017), while the value for $f_3^* f_C f_D$ is
474   an order of magnitude higher than the expected value of 0.0045 for standard rock (Nesterenok & Yakubovich, 2016).
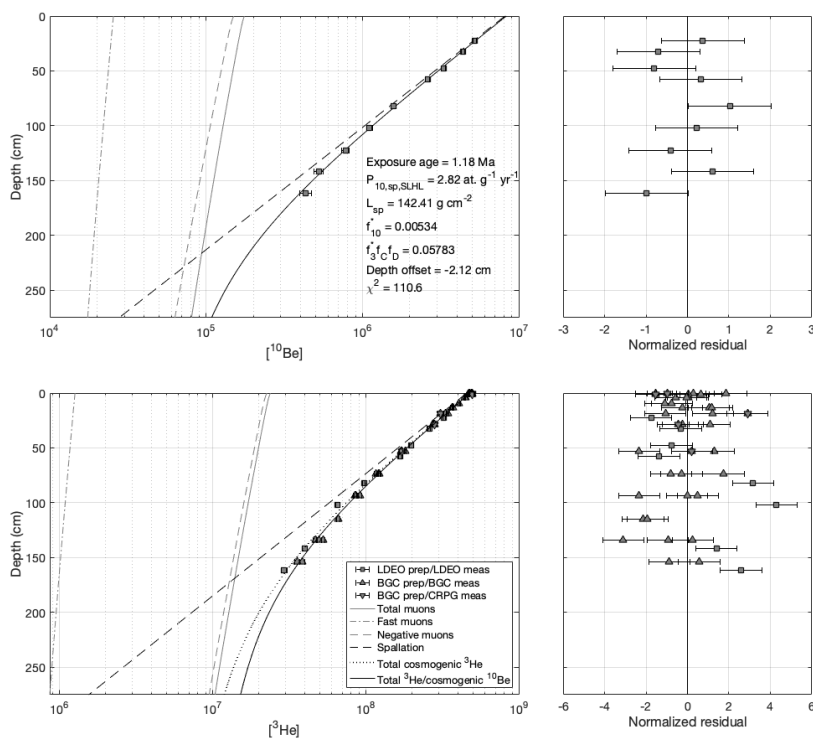475

Figure 5: Model results for Labyrinth core under the zero-erosion assumption. Optimal values for parameters are shown in the text inset in the top left panel.

476 *Steady-erosion end member*

477 For the steady erosion end member, we impose an exposure duration of 14.5 Ma based on ^{39}Ar/^{40}Ar ages on

478 in situ ash deposits that suggest the Labyrinth formed by ~14–15 Ma (Lewis et al., 2006; Sect. 2). With that

479 assumption, the remaining free parameters are ε, $P_{10,sp,SLHL}$, Λ_{sp}, $f_3^* f_C f_D$, and f_{10}^*, and the depth measurement offset

480 below 18 cm. The same fit is achieved as the zero-erosion case, with a minimum value M = 111 for 24 degrees of

481 freedom (reduced χ^2 = 4.6).

482 Fig. 6 gives the results of the steady-erosion exercise. The optimal erosion rate over 14.5 Ma is 41.1 cm Myr^{-}

483 ^{1}, which agrees with the steady-state erosion rate calculated using the measured ^{3}He concentration at the surface (Sect.

484 4.1). Under the steady-erosion assumption, the best-fitting $P_{10,sp,SLHL}$ is 3.36 atoms g^{-1} yr^{-1} and the optimal Λ_{sp} = 144

485 g cm^{-2}. Here, the estimate for $P_{10,sp,SLHL}$ is an upper limit. Notably, the optimal $P_{10,sp,SLHL}$ is close to the estimate of

486 Eaves et al. (2018). The best-fitting value for the depth measurement offset below 18 cm is 2.05 cm.
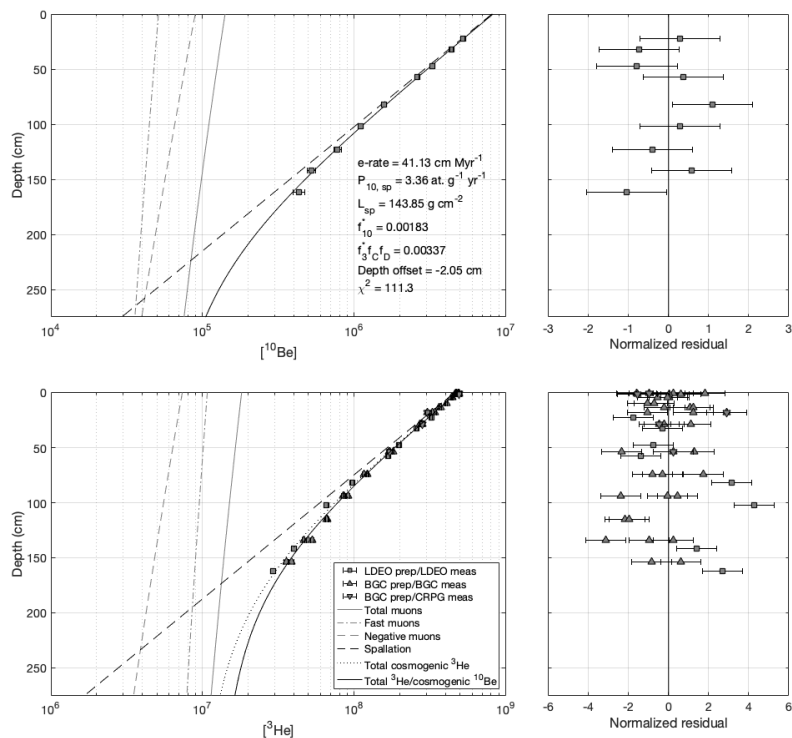
Figure 6: Model results for Labyrinth core for the steady-erosion case. Optimal parameter values are shown in the text inset in the top left panel.

487   The optimal values for parameters related to negative muon capture for the steady-erosion assumption are

488   f_{10}^* = 0.00183 and $f_3^* f_C f_D$ = 0.00337. Here, the value for f_{10}^* is nearly identical as f_{10}^* for quartz (0.00191; Balco, 2017).

489   In this scenario, however, the optimal $f_3^* f_C f_D$ is also the same magnitude as the expected value from standard rock

490   (Nesterenok & Yakubovich, 2016). The fitted values for $P_{10,\ sp,SLHL}$, f_{10}^* and $f_3^* f_C f_D$ for the steady-erosion endmember

491   are closer to the expected values than for the zero-erosion endmember, and there is no geomorphic evidence against

492   steady erosion taking place at the Labyrinth core site. Therefore, going forward, we assume steady erosion for the

493   Labyrinth core and use the muon cross-sections derived under this assumption for calculating muon production rates.

494   **5.1.2 Spallation production in the surface samples**

495   Here, we derive upper and lower limits on the spallation production rate of [10]Be in pyroxene using the [10]Be

496   and [3]He concentrations the six surface samples by again imposing the zero-erosion (lower limit) and steady-erosion

497   (upper limit) end members described in Sect. 5.1.1. All calculations of the muon production rates are made using the

498   "Model 1A" MATLAB code of Balco (2017), with the parameter α set to 1 (Balco, 2017; Borchers et al., 2016), the

499   fast muon reaction cross-sections described in Sect. 5.1.1, and the negative muon capture cross-sections resulting from

500   the steady erosion endmember for the Labyrinth core.

501   For the zero-erosion case, we solve the equation

502
$$P_{10,sp,SLHL,min} = \lambda_{10} * \frac{(N_{10,m} - N_{10,\mu})}{S_{thick} * S_{St} * (1 - e^{-\lambda_{10}t})} \text{ (Equation 12)}$$

503   for each sample. Here, t is the ^{3}He apparent exposure age,

504
$$t = \frac{N_{3,m}}{(P_{3,sp,SLHL} * S_{thick} * S_{St}) + P_{3,\mu}} \text{ (Equation 13)}.$$

505   Where $P_{3,\mu}$ is the total production rate by muons. For the sake of simplicity, we assume that the muon production rate

506   at the center of the sample (sample thickness/2) is equivalent to $P_{3,\mu}$ in the sample (Balco et al., 2008). We then

507   calculate $N_{10, mu}$ by evaluating Equations 7 and 9 using the "Model 1A" MATLAB code for exposure duration t.

508   For the steady-erosion case, we assume that each surface has reached saturation with respect to spallation

509   production and decay. To find the maximum $P_{10,sp,SLHL}$ we solve the equation,

510
$$P_{10,sp,SLHL,max} = (N_{10,m} - N_{10,\mu}) * \frac{(\lambda_{10} + \frac{\varepsilon}{\Lambda_{sp}})}{S_{thick} * S_{St}} \text{ (Equation 14)}$$

511   for each sample. Here, the steady erosion rate ε is estimated for each sample by inverting our measured ^{3}He

512   concentrations using a forward model comprising Equations 1, 4, 6, and 8 and an exposure duration of 14.5 Myr. We

513   again calculate the muon production rate at the sample midpoint, and set $\Lambda_{sp} = 140$, so that the only free parameter in

514   the model is the erosion rate. We fit the model by minimizing the misfit statistic,

515
$$M = \left[\frac{N_{3,p} - N_{3,m}}{\sqrt{\sigma^2_{3,m} + \sigma^2_{3,non-cosmo}}} \right]^2$$

516   The optimal erosion rate is then used in Equation 14 to solve for the upper limit on the ^{10}Be spallation production rate.

517   Together, the zero-erosion and steady-erosion cases yield an allowable range for $P_{10,sp,SLHL}$ given the

518   measured cosmogenic-nuclide concentrations in each surface sample. We take the uncertainty on each value to be the

519   ^{3}He measurement error, ^{10}Be measurement error, and the error on the ^{3}He production rate (11%), propagated in

520   quadrature.

521   Fig. 7 shows the resulting limits for $P_{10,sp,SLHL}$. The minimum values from the zero-erosion end member

522   range from 3.2–3.7 atoms g^{-1} yr^{-1} and the maximum values from the steady-erosion endmember range from 3.9–4.8

523   atoms g^{-1} yr^{-1}. The overall production rate range encompassed by the surface samples (3.2–4.8 atoms g^{-1} yr^{-1}) overlaps

524   with the limits from the Labyrinth core (2.8–3.4 atoms g^{-1} yr^{-1}).

525   **5.1.3 Spallation production rate for ^{10}Be in pyroxene**

526   Now we combine the complementary information derived from the six surface samples and the Labyrinth

527   core to define a summary distribution for $P_{10,sp,SLHL}$ in pyroxene. The true value for $P_{10,sp,SLHL}$ should fall somewhere

528   between the highest of the lower limits, and the lowest of the upper limits, of the whole dataset. Therefore, we assume

529   that there is a uniform probability for all production rate values that fall between these limits. To derive a summary

530   distribution using this assumption, we perform a Monte Carlo simulation with 1e5 iterations. Our summary

531   distribution is described as,

532
$$\sum_{i=1}^{n} \frac{f_i(x)}{\sum f_i(x)} \; where \; f_i(x) = \begin{cases} 1, & max\{P_{10,sp,min,1} \ldots P_{10,sp,min,j}\} < x < min\{P_{10,sp,max,1} \ldots P_{10,sp,max,j}\} \\ 0, & x < max\{P_{10,sp,min,1} \ldots P_{10,sp,min,j}\} \; or \; x > min\{P_{10,sp,max,1} \ldots P_{10,sp,max,j}\} \end{cases}$$

533   Here, x is any potential value for the ^{10}Be production rate. $P_{10,sp,min}$ and $P_{10,sp,max}$ are lower and upper limits,

534   respectively, on the ^{10}Be production rate for sample j. For each Monte Carlo iteration n, $P_{10,sp,min}$ and $P_{10,sp,max}$ are

535   randomly drawn from a normal distribution with the mean and standard deviation of these values found in Sects. 5.1.1

536   and 5.1.2.

537   Fig. 7 shows the resulting summary distribution. The distribution is approximately Gaussian, with a mean of

538   3.6 and a standard deviation of 0.2. Therefore, the likely value for the ^{10}Be spallation production rate in pyroxene from

539   our dataset is 3.6 ± 0.2 atoms g^{-1} yr^{-1}. This agrees with the value of 3.6 ± 0.8 atoms g^{-1} yr^{-1}, cross-calibrated with ^{3}He

540   for samples from the mid-latitudes (Eaves et al., 2018), but offers an improvement on the relative uncertainty of this

541   value from ~20% to ~5%.
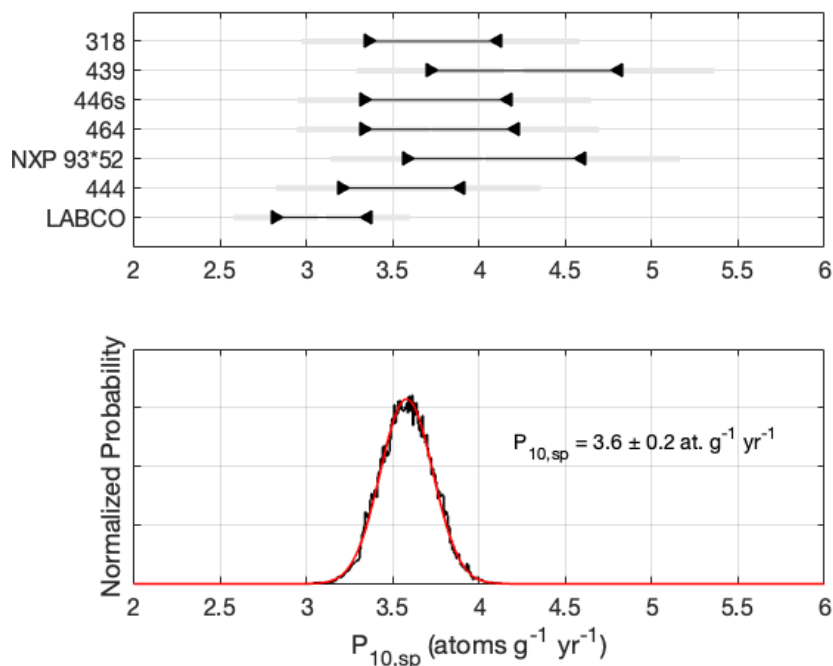
Figure 7: Spallation production rate for ^{10}Be in pyroxene. Top: Minimum and maximum values for $P_{10,sp}$. Gray lines show uncertainty on each value. Bottom: Summary distribution of $P_{10,sp}$. Black line shows results from Monte Carlo simulation described in Sect. 5.1.3. Red line shows the Gaussian distribution constructed using the mean and standard deviation from the Monte Carlo results. Text shows the most likely value for $P_{10,sp}$ given the summary distribution.

5.2 Applications for ^{10}Be in pyroxene

542

543   Based on the presented spallation production rate 3.6 ± 0.2 atoms g^{-1} yr^{-1}, we now explore the potential of

544 ^{10}Be in pyroxene for quantifying ice-sheet and landscape change. On 10^6-year timescales, the relative precision of

545 ^{10}Be in pyroxene ($\sim$2%) allows for simultaneously resolving exposure-ages and erosion-rates using the ^{10}Be-^{3}He pair.

546 Fig. 8 shows a ^{10}Be-^{3}He two-nuclide diagram (e.g., Nishiizumi et al., 1991), constructed using our estimate for the

547 spallation ^{10}Be production rate in pyroxene. Our sample concentrations are located in distinct positions throughout the

548 two-nuclide diagram, generally between the constant exposure and steady-erosion lines, meaning that our samples

549 have experienced a range of erosion rate/exposure duration combinations. With ^{3}He alone, we found apparent

550 (minimum) exposure ages of $\sim$1–6 Ma for the surface samples. Including ^{10}Be shows that those data are better

551 explained with $\sim$2–8 Ma of exposure at erosion rates of $\sim$0–35 cm Myr^{-1}, highlighting the power of this novel two-

552 nuclide approach in pyroxene.

553   Canonically, the Dry Valleys landscape formed $\sim$14.5 Myr ago and has been preserved by extremely low

554 erosion rates since that time (e.g., Denton & Sugden, 2005; Lewis et al., 2006; Sect. 2). Yet, the oldest surface in our

555 dataset is $\sim$8 Ma when considering erosion, with samples 444 and 439 having exposure ages closer to $\sim$2 Ma (except

556 for the Labyrinth core, which we assume has been exposed for 14.5 Myr under steady erosion for the production rate

557 calibration; Sect. 5.1.1). Although our dataset is limited, the fact that several samples have cosmogenic-nuclide

558 concentrations inconsistent with 14.5 Myr of exposure may suggest that the Dry Valleys landscape is more dynamic

559 than once hypothesized, involving either subaerial erosion, burial by ice, or both (Middleton et al., 2012). Applying

560 the ^{10}Be-^{3}He pair in the Dry Valleys and across Antarctica, where much of the exposed rock is mafic Ferrar Dolerite,

561 will yield more accurate exposure histories for understanding ice-sheet and landscape change.

562   In addition to multi-nuclide applications, an obvious use of ^{10}Be in pyroxene is surface exposure dating. At

563 the sample sizes used in this study (0.1–0.2 g pyroxene), ^{10}Be in pyroxene is an ideal exposure chronometer in

564 landscapes like the Dry Valleys, where, owing to long exposure durations at low erosion rates, ^{10}Be concentrations

565 are high ($\sim$$10^6$–$10^7$ atoms g^{-1}). Applying ^{10}Be in pyroxene for younger landscapes, however, would require increasing

566 the sample size. Eaves et al. (2018), successfully extracted beryllium from 1–2 g of pyroxene using larger resin

567 volumes for cation exchange chromatography than we used here, so an increase to 2 g (or more) of pyroxene is likely

568 possible by combining our pH 8 precipitation step with slightly larger cation resin volumes. Using the relative

569 uncertainties associated with our reported ^{10}Be concentrations (Table S1; Sect. 3.2.3) and assuming 2 g as a plausible

570 larger sample size, we can estimate the relative uncertainties related to different exposure durations. To achieve

571 relative uncertainties of $\sim$5%, we would need to measure $\sim$1.2 x 10^5 atoms of ^{10}Be (Fig. S3). At a sample size of 2 g,

572 this equates to 6 x 10^4 atoms g^{-1}, or $\sim$17 ka at high-latitude sea level and $\sim$4 ka at 2000 m elevation at high latitude. A

573 threshold of 15% uncertainty would require measurement of 3 x 10^4 atoms of ^{10}Be, or, at 2 g of pyroxene, a ^{10}Be

574 concentration of 1.5 x 10^4 atoms g^{-1}. This is equal to $\sim$4 ka at high-latitude sea level or $\sim$1 ka at 2000 m elevation at

575 high latitude. A prime target area for applying ^{10}Be in pyroxene to evaluate glacier change in the Late Holocene is the

576 high-altitude tropical Andes, where moraine boulders are derived from pyroxene-bearing lava flows (e.g., Bromley et

577 al., 2011). Using 2g of pyroxene from moraines at 4000 m elevation in the tropics, would yield 5% uncertainty for

578 exposure ages of 2 ka and 15% uncertainty for exposure ages of 500 years. Importantly, the number of ^{10}Be atoms

579   associated with both of these uncertainty thresholds is greater than the average number of ^{10}Be atoms in our blanks

580   (5.7 x 10^3 ^{10}Be atoms; Table S2). Therefore, a relatively modest increase in the sample size used here would therefore

581   make ^{10}Be exposure dating in pyroxene useful in landscapes with Last Glacial Maximum to Late Holocene exposure
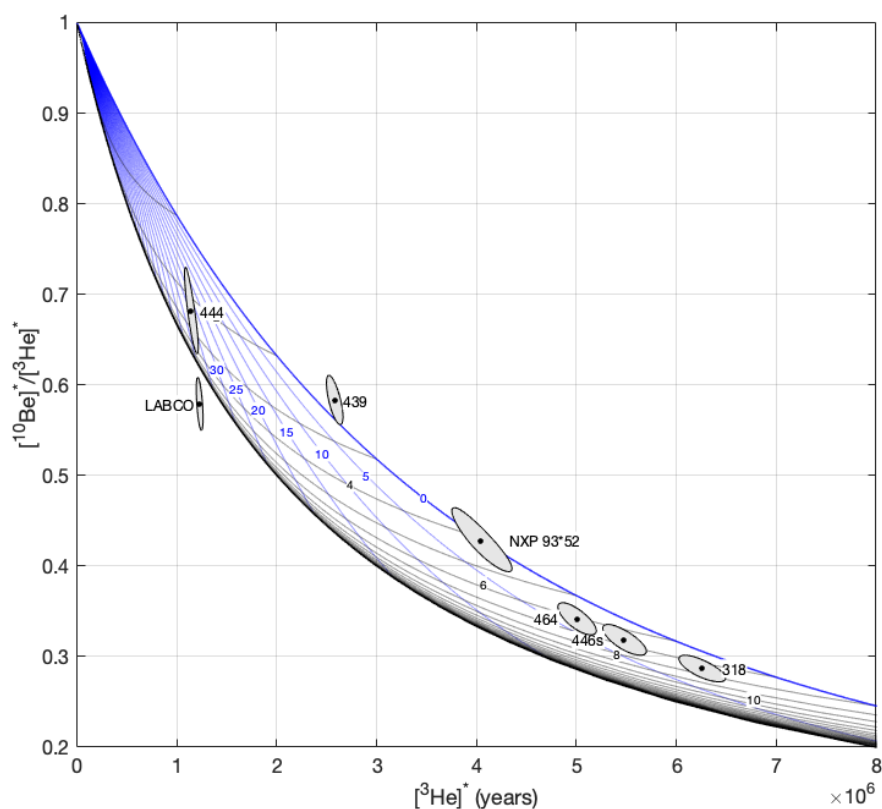
582   ages.

Figure 8: ^{10}Be-^{3}He two-nuclide diagram. Asterisks indicate that nuclide concentrations have been normalized using site-specific production rates for each sample for ease of comparison across sampling locations. The x-axis therefore represents apparent ^{3}He years. Production by muons is not included, as a steady erosion line that includes muons changes with elevation. Ellipses show 68% confidence intervals based on measurement uncertainties. The ^{10}Be concentration for the Labyrinth core surface (LABCO) sample is taken from the modeled surface concentration under the steady erosion assumption for the Labyrinth core (Fig. 6) with a conservative 3% uncertainty. Note that the LABCO concentrations would fall near a steady erosion line drawn with muons included for elevation of the Labyrinth core, as the ^{10}Be concentration was derived from the modeled steady-state erosion endmember with 14.5 Myr of exposure. The top line (blue) bounding the steady-erosion island is the simple exposure line and the bottom bounding line (black) is the steady erosion line. Blue lines are lines of constant erosion and black lines are lines of constant age. The diagram shows that measured ^{10}Be and ^{3}He concentrations in the surface samples are consistent with ~2–8 Ma of exposure and ~0–35 cm Myr^{-1} erosion.

583 **6 Conclusions**

584   We measured ^{10}Be in Ferrar Dolerite pyroxenes from the McMurdo Dry Valleys, Antarctica with apparent

585 ^{3}He exposure ages of 1–6 Ma. To facilitate the beryllium isolation from pyroxene, we added a pH 8 precipitation to

586 remove Ca, Mg, Na, reducing the cation load prior to ion exchange chromatography. We also found that with ~20%

587 sample dissolution through HF leaching, ^{10}Be concentrations stabilized, suggesting complete removal of meteoric

588 ^{10}Be, even in our samples with 10^6-year exposure durations. Our ^{10}Be/^{9}Be ratios ranged from 5 x 10^{-13} to 4 x 10^{-15} for

589 samples with ^{10}Be concentrations from 4 x 10^{-15} to 6 x 10^{-13} atoms g^{-1}, with relative uncertainties of 2–9%. The average

590 blank contained 5.7 x 10^3 atoms ^{10}Be, and blank corrections ranged from <1% in the surface samples to 7% at 1.6 m

591 depth in the Labyrinth bedrock core. We derived a ^{10}Be spallation production rate in pyroxene of 3.6 ± 0.2 atoms g^{-1}

592 yr^{-1} using ^{10}Be and ^{3}He concentrations in the six surface samples and the Labyrinth drill core. Our analysis of the

593 Labyrinth core also yields the first direct constraints of the cross-sections for ^{10}Be and ^{3}He production by negative

594 muon capture ($f_{10}^* = 0.00183$ and $f_3^* f_C f_D = 0.00337$).

595   Given the measurement precision, low ^{10}Be laboratory blanks and the production rate reported here, ^{10}Be in

596 pyroxene can now be applied for surface exposure dating, burial dating, and erosion quantification. For example, we

597 estimate that surfaces exposed for 2 ka at 4000 m in the Tropical Andes could be dated with 5% uncertainty using our

598 beryllium extraction methods for pyroxene. Furthermore, the application of the ^{10}Be-^{3}He pair in pyroxene reveals that

599 our cosmogenic-nuclide concentrations in surface samples located throughout the Antarctic Dry Valleys are consistent

600 with ~2–8 Ma of exposure at 0–35 cm Myr^{-1}, offering more insight into the ice-sheet and denudation histories of the

601 Dry Valleys than does ^{3}He alone. With this dataset, we observe that locations throughout the Dry Valleys have a range

602 of exposure and erosional histories. Expanding the use of the ^{10}Be-^{3}He pair beyond surfaces that appear stable/low-

603 erosion will yield further insight into this Antarctic landscape that is likely more dynamic than once hypothesized. In

604 Antarctica and beyond, the ^{10}Be-^{3}He nuclide pair opens new opportunities for more accurately quantifying glacier and

605 landscape histories in mafic rocks.

606

615 .

616 **Data and Code Availability.** All analytical information associated with cosmogenic-nuclide measurements appear in

617 the tables and Supplementary Information. All MATLAB scripts used for model fitting and to generate the figures

618 can be found at https://github.com/alliebalter-kennedy/be-ten-pyx.

619

620 **Author Contribution Statement.** ABK, RS, GB, BT carried out sample preparation. ABK and RS performed

621 beryllium extraction. GB, GW, JL, LP, BT, PHB performed helium analysis, and beryllium measurements were

622 performed by AJH. ABK and GB performed data analysis. ABK prepared the manuscript with contributions from

623 JMS, GB, RS, GW, JM, JLL, AJH, and PHB.

624

625 **Competing Interests.** GB is an editor of Geochronology.

626 **References**

627 Ackert, Robert P. (2000). *Antarctic glacial chronology: new constraints from surface exposure dating* [Doctoral
628   Dissertation, Massachusetts Institute of Technology and the Woods Hole Oceanographic Institution]. doi:
629   10.1575/1912/4123
630 Ackert, R.P, & Kurz, M. D. (2004). Age and uplift rates of Sirius Group sediments in the Dominion Range,
631   Antarctica, from surface exposure dating and geomorphology. *Global and Planetary Change*, *42*(1–4),
632   207–225. doi: 10.1016/j.gloplacha.2004.02.001
633 Andrews, J. N., & Kay, R. L. F. (1982). Natural production of tritium in permeable rocks. *Nature*, *298*(5872), 361–
634   363. doi: 10.1038/298361a0
635 Argento, D. C., Stone, J. O., Reedy, R. C., & O'Brien, K. (2015). Physics-based modeling of cosmogenic nuclides
636   part II – Key aspects of in-situ cosmogenic nuclide production. *Quaternary Geochronology*, *26*, 44–55. doi:
637   10.1016/j.quageo.2014.09.005
638 Balco, G. (2017). Production rate calculations for cosmic-ray-muon-produced 10Be and 26Al benchmarked against
639   geological calibration data. Quaternary Geochronology, *39*, 150–173. doi: 10.1016/j.quageo.2017.02.001
640 Balco, G. (2020, August 22). Noncosmogenic helium-3 in pyroxene and Antarctic exposure dating. Retrieved June
641   *23*, 2022, from Cosmognosis: The Bleeding Edge of Cosmogenic-Nuclide Geochemistry website:
642   https://cosmognosis.wordpress.com/2020/08/22/noncosmogenic-helium-3-in-pyroxene-and-antarctic-
643   exposure-dating/
644 Balco, G., Blard, P.-H., Shuster, D. L., Stone, J. O. H., & Zimmermann, L. (2019). Cosmogenic and nucleogenic
645   21Ne in quartz in a 28-meter sandstone core from the McMurdo Dry Valleys, Antarctica. Quaternary
646   Geochronology, *52*, 63–76. doi: 10.1016/j.quageo.2019.02.006
647 Balco, G., & Rovey, C. W. (2010). Absolute chronology for major Pleistocene advances of the Laurentide Ice Sheet.
648   *Geology*, *38*(9), 795–798. doi: 10.1130/g30946.1
649   Balco, G., & Shuster, D. L. (2009). 26Al–10Be–21Ne burial dating. *Earth and Planetary Science Letters*,
650   *286*(3–4), 570–575. doi: 10.1016/j.epsl.*200*9.07.025
651 Balco, G., Stone, J. O., Lifton, N. A., & Dunai, T. J. (2008). A complete and easily accessible means of calculating
652   surface exposure ages or erosion rates from 10Be and 26Al measurements. Quaternary Geochronology,
653   3(3), 174–195. doi: 10.1016/j.quageo.2007.12.001
654 Balter-Kennedy, A., Bromley, G., Balco, G., Thomas, H., & Jackson, M. S. (2020). A 14.5-million-year record of
655   East Antarctic Ice Sheet fluctuations from the central Transantarctic Mountains, constrained with
656   cosmogenic 3He, 10Be, 21Ne, and 26Al. *The Cryosphere*, *14*(8), 2647–2672. doi: 10.5194/tc-14-2647-
657   2020
658 Bindschadler, R., Vornberger, P., Fleming, A., Fox, A., Mullins, J., Binnie, D., … Gorodetzky, D. (2008). The
659   Landsat Image Mosaic of Antarctica. *Remote Sensing of Environment*, *112*(12), 4214–4226. doi:
660   10.1016/j.rse.2008.07.006
661 Blard, P.-H. (2021). Cosmogenic 3He in terrestrial rocks: A review. *Chemical Geology*, *586*, 120543. doi:
662   10.1016/j.chemgeo.2021.120543
663 Blard, P.-H., Balco, G., Burnard, P. G., Farley, K. A., Fenton, C. R., Friedrich, R., … Zimmermann, L. (2015). An
664   inter-laboratory comparison of cosmogenic 3He and radiogenic 4He in the CRONUS-P pyroxene standard.
665   Quaternary Geochronology, 26, 11–19. doi: 10.1016/j.quageo.2014.08.004
666 Blard, P.-H., Bourlès, D., Pik, R., & Lavé, J. (2008). In situ cosmogenic 10Be in olivines and pyroxenes. Quaternary
667   Geochronology, 3(3), 196–205. doi: 10.1016/j.quageo.2007.11.006
668 Borchers, B., Marrero, S., Balco, G., Caffee, M., Goehring, B., Lifton, N., … Stone, J. (2016). Geological
669   calibration of spallation production rates in the CRONUS-Earth project. Quaternary Geochronology, *31*,

670   188–1*98*. doi: 10.1016/j.quageo.2015.01.009
671 Bromley, G. R. M., Hall, B. L., Schaefer, J. M., Winckler, G., Todd, C. E., & Rademaker, K. M. (2011). Glacier
672   fluctuations in the southern Peruvian Andes during the late-glacial period, constrained with cosmogenic
673   3He. *Journal of Quaternary Science*, *26*(1), 37–43. doi: 10.1002/jqs.1424
674 Bromley, G. R. M., Winckler, G., Schaefer, J. M., Kaplan, M. R., Licht, K. J., & Hall, B. L. (2014). Pyroxene
675   separation by HF leaching and its impact on helium surface-exposure dating. Quaternary Geochronology,
676   *23*, 1–8. doi: 10.1016/j.quageo.2014.04.003
677 Bruno, L. A., Baur, H., Graf, T., Schlüchter, C., Signer, P., & Wieler, R. (1997). Dating of Sirius Group tillites in
678   the Antarctic Dry Valleys with cosmogenic 3He and21Ne. Earth and Planetary Science Letters, *147*(1–4),
679   37–54. doi: 10.1016/s0012-821x(97)00003-4
680 Cerling, T. (1994). *Geomorphology* and In-Situ Cosmogenic Isotopes. *Annual Review of Earth and Planetary
681   Sciences*, *22*(1), 273–317. doi: 10.1146/annurev.earth.22.1.273
682 Cerling, T. E. (1990). Dating geomorphologic surfaces using cosmogenic 3He. *Quaternary Research*, *33*(2), 1*48*–
683   156. doi: 10.1016/0033-5894(90)90015-d
684 Chmeleff, J., Blanckenburg, F. von, Kossert, K., & Jakob, D. (2010). Determination of the 10Be half-life by
685   multicollector ICP-MS and liquid scintillation counting. *Nuclear Instruments and Methods in Physics
686   Research Section B: Beam Interactions with Materials and Atoms*, *268*(2), 192–199. doi:
687   10.1016/j.nimb.2009.09.012
688 Denton, G. H., & Sugden, D. E. (2005). Meltwater features that suggest Miocene ice-sheet overriding of the
689   Transantarctic Mountains in Victoria Land, Antarctica. *Geografiska Annaler: Series A, Physical
690   Geography*, *87*(1), 67–85. doi: 10.1111/j.0435-3676.2005.002*45*.x
691 Denton, G. H., Sugden, D. E., Marchant, D. R., Hall, B. L., & Wilch, T. I. (1993). East Antarctic Ice Sheet
692   Sensitivity to Pliocene Climatic Change from a Dry Valleys Perspective. *Geografiska Annaler. Series A,
693   Physical Geography*, *75*(4), 155. doi: 10.*230*7/521200
694 Dunai, T. J. (2010). *Cosmogenic Nuclides*. doi: 10.1017/cbo9780511804519
695 Eaves, S. R., Collins, J. A., Jones, R. S., Norton, K. P., Tims, S. G., & Mackintosh, A. N. (2018). Further constraint
696   of the in situ cosmogenic 10Be production rate in pyroxene and a viability test for late Quaternary exposure
697   dating. Quaternary Geochronology, 48, 121–132. doi: 10.1016/j.quageo.2018.09.006
698 von Egidy, T., & Hartmann, F. J. (1982). Average muonic Coulomb capture probabilities for 65 elements. *Physical
699   Review A*, *26*(5), 2*355*–2360. doi: 10.1103/physreva.26.2355
700 Fink, D., & Smith, A. (2007). An inter-comparison of 10Be and 26Al AMS reference standards and the 10Be half-
701   life. Nuclear Instruments and Methods in Physics Research Section B: Beam Interactions with Materials
702   and Atoms, *259*(1), 600–609. doi: 10.1016/j.nimb.2007.01.299
703 Gosse, J. C., & Phillips, F. M. (2001). Terrestrial in situ cosmogenic nuclides: theory and application. *Quaternary
704   Science Reviews*, *20*(14), 1475–1560. doi: 10.1016/s0277-3791(00)00171-2
705 Granger, D. E. (2006). A review of burial dating methods using 26Al and 10Be. In L. L. Siame, D. L. Bourlès, &
706   Brown (Eds.), *In Situ-Produced Cosmogenic Nuclides and Quantification of Geological Processes:
707   Geological Society of America Special Paper 415* (pp. 1–16). doi: 10.1130/2006.2415(01)
708 Heisinger, B., Lal, D., Jull, A. J. T., Kubik, P., Ivy-Ochs, S., Neumaier, S., … Nolte, E. (2002a). Production of
709   selected cosmogenic radionuclides by muons 1. Fast muons. Earth and Planetary Science Letters, 200(3–4),
710   3*45*–355. doi: 10.1016/s0012-821x(02)00640-4
711 Heisinger, B., Lal, D., Jull, A. J. T., Kubik, P., Ivy-Ochs, S., Knie, K., & Nolte, E. (2002b). Production of selected
712   cosmogenic radionuclides by muons: 2. Capture of negative muons. Earth and Planetary Science Letters,
713   200(3–4), 357–369. doi: 10.1016/s0012-821x(02)00641-6
714 Hippe, K. (2017). Constraining processes of landscape change with combined in situ cosmogenic 14C-10Be
715   analysis. Quaternary Science Reviews, *173*, 1–19. doi: 10.1016/j.quascirev.2017.07.020
716 Ivy-Ochs, S., Kubik, P. W., Masarik, J., Wieler, R., Bruno, L., & Schlüchter, C. (1998). Preliminary results on the
717   use of pyroxene fro 10Be surface exposure dating. *Schweizerische Mineralogische Und Petrographische
718   Mitteilungen*, (78), 375–382.
719 Ivy-Ochs, S., Schlüchter, C., Kubik, P. W., Dittrich-Hannen, B., & Beer, J. (1995). Minimum 10Be exposure ages of
720   early Pliocene for the Table Mountain plateau and the Sirius Group at Mount Fleming, Dry Valleys,
721   Antarctica. Geology, 23(11), 1007–1010. doi: 10.1130/0091-7613(1995)023<1007:mbeaoe>2.3.co;2
722 Kaplan, M. R., Licht, K. J., Winckler, G., Schaefer, J. M., Bader, N., Mathieson, C., … Graly, J. A. (2017). Middle
723   to Late Pleistocene stability of the central East Antarctic Ice Sheet at the head of Law Glacier. Geology,
724   45(11), 963–966. doi: 10.1130/g39189.1
725 Kohl, C. P., & Nishiizumi, K. (1992). Chemical isolation of quartz for measurement of in-situ -produced

726   cosmogenic nuclides. *Geochimica et Cosmochimica Acta*, *56*(9), 3583–3587. doi: 10.1016/0016-
727   7037(92)90401-4
728   Korschinek, G., Bergmaier, A., Faestermann, T., Gerstmann, U. C., Knie, K., Rugel, G., Wallner, A., Dillmann, I.,
729   Dollinger, G., Gostomski, Ch. L. von, Kossert, K., Maiti, M., Poutivtsev, M., & Remmert, A. (2010). A
730   new value for the half-life of 10Be by Heavy-Ion Elastic Recoil Detection and liquid scintillation counting.
731   *Nuclear Instruments and Methods in Physics Research Section B: Beam Interactions with Materials and*
732   *Atoms*, *268*(2), 187–191. https://doi.org/10.1016/j.nimb.2009.09.020
733   Kurz, M. D., & Brook, E. J. (1994). Surface exposure dating with cosmogenic nuclides. In *Dating in exposed and*
734   *surface contexts* (pp. 139–159).
735   Lal, D. (1987). Production of 3He in terrestrial rocks. *Chemical Geology: Isotope Geoscience Section*, *66*(1–2), 89–
736   98. doi: 10.1016/0168-9622(87)90031-5
737   Lal, D. (1991). Cosmic ray labeling of erosion surfaces: in situ nuclide production rates and erosion models. Earth
738   and Planetary Science Letters, *104*(2–4), 424–439. doi: 10.1016/0012-821x(91)90220-c
739   Lamp, J. L., Marchant, D. R., Mackay, S. L., & Head, J. W. (2017). Thermal stress weathering and the spalling of
740   Antarctic rocks. *Journal of Geophysical Research: Earth Surface*, *122*(1), 3–24. doi:
741   10.1002/2016jf003992
742   Larsen, I. J., Farley, K. A., Lamb, M. P., & Pritchard, C. J. (2021). Empirical evidence for cosmogenic 3He
743   production by muons. Earth and Planetary Science Letters, *562*, 116825. doi: 10.1016/j.epsl.2021.116825
744   Lewis, A. R., Marchant, D. R., Kowalewski, D. E., Baldwin, S. L., & Webb, L. E. (2006). The age and origin of the
745   Labyrinth, western Dry Valleys, Antarctica: Evidence for extensive middle Miocene subglacial floods and
746   freshwater discharge to the Southern Ocean. Geology, 34(7), 513–516. doi: 10.1130/g22145.1
747   Margerison, H. R., Phillips, W. M., Stuart, F. M., & Sugden, D. E. (2005). Cosmogenic 3He concentrations in
748   ancient flood deposits from the Coombs Hills, northern Dry Valleys, East Antarctica: interpreting exposure
749   ages and erosion rates. Earth and Planetary Science Letters, 230(1–2), 163–175. doi:
750   10.1016/j.epsl.2004.11.007
751   Matsuda, J., Matsumoto, T., Sumino, H., Nagao, K., Yamamoto, J., Miura, Y., … Sano, Y. (2002). The 3He/4He
752   ratio of the new internal He Standard of Japan (HESJ). *GEOCHEMICAL JOURNAL*, *36*(2), 191–195. doi:
753   10.2343/geochemj.36.191
754   Matsuoka, K., Skoglund, A., Roth, G., Pomereu, J. de, Griffiths, H., Headland, R., … Melvær, Y. (2021).
755   Quantarctica, an integrated mapping environment for Antarctica, the Southern Ocean, and sub-Antarctic
756   islands. *Environmental Modelling & Software*, *140*, 105015. doi: 10.1016/j.envsoft.2021.105015
757   Middleton, J. L., Ackert, R. P., & Mukhopadhyay, S. (2012). Pothole and channel system formation in the McMurdo
758   Dry Valleys of Antarctica: New insights from cosmogenic nuclides. Earth and Planetary Science Letters,
759   355, 341–350. doi: 10.1016/j.epsl.2012.08.017
760   Nespolo, M. (2020). *Reference Module in Earth Systems and Environmental Sciences*. (American Mineralogist 89
761   2004), 287–296. doi: 10.1016/b978-0-12-409548-9.12409-1
762   Nesterenok, A. V., & Yakubovich, O. V. (2016). Production of ^{3}He in Rocks by Reactions Induced by Particles
763   of the Nuclear-Active and Muon Components of Cosmic Rays: Geological and Petrological Implications.
764   *ArXiv*. doi: 10.48550/arxiv.1607.08770
765   Niedermann, S., Schaefer, J. M., Wieler, R., & Naumann, R. (2007). The production rate of cosmogenic 38Ar from
766   calcium in terrestrial pyroxene. Earth and Planetary Science Letters, *257*(3–4), 596–608. doi:
767   10.1016/j.epsl.2007.03.020
768   Nishiizumi, K., Klein, J., Middleton, R., & Craig, H. (1990). Cosmogenic10Be,26Al, and3He in olivine from Maui
769   lavas. Earth and Planetary Science Letters, 98(3–4), 263–266. doi: 10.1016/0012-821x(90)90028-v
770   Nishiizumi, K., Kohl, C. P., Arnold, J. R., Klein, J., Fink, D., & Middleton, R. (1991). Cosmic ray produced 10Be
771   and 26Al in Antarctic rocks: exposure and erosion history. Earth and Planetary Science Letters, 104(2–4),
772   440–454. doi: 10.1016/0012-821x(91)90221-3
773   Nishiizumi, Kunihiko, Imamura, M., Caffee, M. W., Southon, J. R., Finkel, R. C., & McAninch, J. (2007). Absolute
774   calibration of 10Be AMS standards. Nuclear Instruments and Methods in Physics Research Section B:
775   Beam Interactions with Materials and Atoms, *258*(2), 403–413. doi: 10.1016/j.nimb.2007.01.297
776   Schaefer, J. M., Codilean, A. T., Willenbring, J. K., Lu, Z.-T., Keisling, B., Fülöp, R.-H., & Val, P. (2022).
777   Cosmogenic nuclide techniques. *Nature Reviews Methods Primers*, *2*(1), 18. doi: 10.1038/s43586-022-
778   00096-9
779   Schaefer, J. M., Denton, G. H., Kaplan, M., Putnam, A., Finkel, R. C., Barrell, D. J. A., … Schlüchter, C. (2009).
780   High-Frequency Holocene Glacier Fluctuations in New Zealand Differ from the Northern Signature.
781   Science, *324*(5927), 622–625. doi: 10.1126/science.1169312

782 Schaefer, J. M., Faestermann, T., Herzog, G. F., Knie, K., Korschinek, G., Masarik, J., … Winckler, G. (2006).
783   Terrestrial manganese-53 — A new monitor of Earth surface processes. Earth and Planetary Science
784   Letters, *251*(3–4), 334–345. doi: 10.1016/j.epsl.2006.09.016
785 Schaefer, J. M., Finkel, R. C., Balco, G., Alley, R. B., Caffee, M. W., Briner, J. P., … Schwartz, R. (2016).
786   Greenland was nearly ice-free for extended periods during the Pleistocene. Nature, *540*(7632), 252–255.
787   doi: 10.1038/nature20146
788 Schaefer, J. M., Winckler, G., Blard, P.-H., Balco, G., Shuster, D. L., Friedrich, R., … Schluechter, C. (2016).
789   Performance of CRONUS-P – A pyroxene reference material for helium isotope analysis. Quaternary
790   Geochronology, 31, 237–239. doi: 10.1016/j.quageo.2014.07.006
791 Schäfer, J. M., Ivy-Ochs, S., Wieler, R., Leya, I., Baur, H., Denton, G. H., & Schlüchter, C. (1999). Cosmogenic
792   noble gas studies in the oldest landscape on earth: surface exposure ages of the Dry Valleys, Antarctica.
793   Earth and Planetary Science Letters, *167*(3–4), 215–226. doi: 10.1016/s0012-821x(99)00029-1
794 Stone, J. O. (2000). Air pressure and cosmogenic isotope production. *Journal of Geophysical Research: Solid Earth*,
795   *105*(B10), 23753–23759. doi: 10.1029/2000jb900181
796 Sugden, D. E., Marchant, D. R., Potter, N., Souchez, R. A., Denton, G. H., III, C. C. S., & Tison, J.-L. (1995).
797   Preservation of Miocene glacier ice in East Antarctica. Nature, *376*(6539), 412–414. doi:
798   10.1038/376412a0
799 Summerfield, M. A., Stuart, F. M., Cockburn, H. A. P., Sugden, D. E., Denton, G. H., Dunai, T., & Marchant, D. R.
800   (1999). Long-term rates of denudation in the Dry Valleys, Transantarctic Mountains, southern Victoria
801   Land, Antarctica based on in-situ-produced cosmogenic 21Ne. Geomorphology, 27(1–2), 113–129. doi:
802   10.1016/s0169-555x(98)00093-2
803 Suzuki, T., Measday, D. F., & Roalsvig, J. P. (1987). Total nuclear capture rates for negative muons. *Phys. Rev. C*,
804   *35*, 2212–2224. https://doi.org/10.1103/PhysRevC.35.2212
805 United States Geological Survey. *Taylor Glacier* [map] 1:250,000. USGS 1:250,000 Topographic Reconnaissance
806   Series (Topographic), sheet ST 57-60/5. Reston, VA: The Survey, 1988.
807 Winckler, G., R.F. Anderson, & P. Schlosser (2005). Equatorial Pacific productivity and dust flux during the Mid-
808   Pleistocene Climate Transition, Paleoceanography, Vol. 20, No.4, PA4025, doi: 10.1029/2005PA001177
809 Young, N. E., Lesnek, A. J., Cuzzone, J. K., Briner, J. P., Badgeley, J. A., Balter-Kennedy, A., … Schaefer, J. M.
810   (2021). In situ cosmogenic 10Be–14C–26Al measurements from recently deglaciated bedrock as a new tool
811   to decipher changes in Greenland Ice Sheet size. *Climate of the Past*, *17*(1), 419–450. doi: 10.5194/cp-17-
812   419-2021
813 Zavala, K., Leitch, A. M., & Fisher, G. W. (2011). Silicic Segregations of the Ferrar Dolerite Sills, Antarctica.
814   *Journal of Petrology*, *52*(10), 1927–1964. doi: 10.1093/petrology/egr035
815 Zimmermann, L., Avice, G., Blard, P.-H., Marty, B., Füri, E., & Burnard, P. G. (2018). A new all-metal induction
816   furnace for noble gas extraction. Chemical Geology, *480*, 86–92. doi: 10.1016/j.chemgeo.2017.09.018